

Phase Behavior and Solvation Properties in Inhomogeneous Fluids

Kiharu ABE

Division of Earth, Life, and Molecular Sciences
Graduate School of Natural Science and Technology
Okayama University

2015

Contents

General Introduction	1
Background	1
Molecular Simulation	2
Confined fluids	3
Statistical mechanics of solvation	10
Outline of the present study	19
1 Model of Freezing Behavior of Liquid Monolayers Adsorbed in Cylindrical Pores	23
1.1 Abstract	23
1.2 Introduction	23
1.3 Model	24
1.4 Isotropic model: Effect of pore diameter on freezing	29
1.5 Anisotropic model: Effect of anisotropy on freezing	32
2 Local solubility of nonpolar molecules in the liquid-vapor interfaces of water and simple liquids	37
2.1 Abstract	37
2.2 Introduction	38
2.3 Theory	40
2.4 Methods	41
2.5 Results	42
3 Temperature dependence of local solubility of hydrophobic molecules in the liquid-vapor interface of water	55

3.1	Abstract	55
3.2	Introduction	56
3.3	Theoretical background	58
3.4	Model systems	60
3.5	Method	61
3.6	Results	63
3.7	Summary	71
	Summary	77
	List of Publications	81
	Acknowledgments	83

General Introduction

Background

The field of theoretical study on physical and chemical properties of fluids and solids had seen a great progress in technique with the advent of molecular simulation. Since then, numerically exact calculation of properties of an assembly of a large number of molecules has been available. Molecular simulation is used for the study of structure, phase behavior, chemical reaction, solvation properties, and dynamical properties, etc. Recently, there are an increasing number of studies on the physical properties of inhomogeneous fluids. This seems to be related to a growing interest in the molecular-level understanding of phenomena in biological systems, where the surrounding environment is far from homogeneous. One of the most crucial sources of the complexity in such systems is the spacial inhomogeneity. Consequently, any local property of an inhomogeneous system depends on the position. Molecular simulation serves as a powerful method to study both macroscopic and microscopic properties of inhomogeneous fluids. In this thesis, theoretical and computer-simulation studies on phase behavior and solvation properties of two concrete systems of inhomogeneous fluids are presented.

In a homogeneous or bulk fluid, any equilibrium properties are independent of the position in the system. For example, the average number density of the molecules in any partial volume in the whole system is N/V , the total number of the molecules divided by the total volume. The homogeneous density distribution breaks down if the fluid is exposed to an external field, such as gravitational field, electric field, and fluid molecule-wall potential, etc. The equilibrium density distribution has the same symmetry as that of the external field. For example, the local number density of a noninteracting gas under gravitational field is a monotonically decreasing function of the height. The container wall may also be a source of the external field. The nature of fluid

molecule-wall interaction depends on the chemical properties, roughness, and geometry of the wall. Inhomogeneity in fluids may be induced without an external field. For example, the spontaneous phase separation to gas and liquid phases, which is caused by the change in thermodynamic conditions, yields a thin inhomogeneous interfacial region between them. The structure in the interfacial region is different from those of gas and liquid phases. Near the triple point, the width of the interfacial region is of the order of several molecular diameters.

Molecular Simulation

By using molecular simulation, a huge number of molecular configurations of a system is obtained from a single initial configuration. For a system of N monatomic molecules, the configuration is specified by $3N$ coordinates $x_1, y_1, z_1, \dots, x_N, y_N, z_N$. An ultimate purpose of molecular simulation is to calculate the motion of all constituent molecules. This role is played by Molecular Dynamics (MD) simulation. In this method, the new configuration after the time Δt (~ 1 fs) is determined by numerically solving the Newtonian equation of motion. By repeating this, in principle, the time evolution of the position and velocity of each particle can be obtained. Any dynamical properties can be extracted from the obtained trajectory.

If the target properties are static ones in the equilibrium state, the sequence of the obtained configurations does not need to be consistent with real motion. Instead, their probability distribution should be consistent with the statistical mechanical ensemble of interest. In the canonical ensemble, for example, the ratio of the probability of observing one particular configuration with the potential energy U_1 to that of observing another particular configuration with the potential energy U_2 should be $\exp[-(U_1 - U_2)/kT]$, where T is temperature and k is Boltzmann's constant. For this purpose, another method of simulation, the Monte Carlo (MC) method, can be used. In this method, a set of configurations is generated in a stochastic way based on the theory of Markov processes. If an appropriate transition matrix is used, configuration set with any desired distribution can be obtained. There is no concept of time in MC method, therefore this method cannot be used to study dynamical properties. An advantage of MC method is that any type of microscopic state is allowed as long as the Hamiltonian is given as a function of the microscopic state. Therefore, MC method can be applied not only to continuous models but also to discrete models such as lattice models.

MD method can also generate a set of configurations that is consistent with canonical ensemble, if one constructs the so-called ‘extended system’ in which the Hamiltonian of the system of interest is modified with an additional degree of freedom. This methodology is developed by Nosé [1], and further extended to deal with the isothermal-isobaric ensemble [2].

Although, in principle, any molecular-level information can be obtained from molecular simulation, there is always the problem of calculation time. The seriousness of this problem depends on the system size (i.e., the total number of interaction sites), thermodynamic state, and the property of interest. For a three-dimensional system with a fixed number density, the number of molecules is proportional to the cube of the cell length. Also, a considerable amount of time may be required to achieve the equilibrium state. For example, with a standard method, reproducing a solid-to-solid or fluid-to-solid phase change in a dense material at low temperatures is very difficult. It is also hard to simulate a system near the critical point where the correlation length and the relaxation time may exceed the cell length and the calculation time, respectively. Nevertheless, for systems with a moderate inhomogeneity at moderate thermodynamic conditions, reliable results can be obtained by simulation with a practical cell size and calculation time.

Confined fluids

When a porous material is exposed to a fluid, some of the fluid molecules are adsorbed inside the pore space of the material. This is an example of confined fluids, the molecules of which are limited in a small space. The allowed space for the confined fluid is specified by the pore geometry of the confining material. The nature of the interaction between the pore surface and fluid molecules also affects the properties of confined fluids. Most of the thermodynamic properties of confined fluids are quantitatively and/or qualitatively different from those of bulk fluids. It is known that the melting point of a confined material is shifted higher or lower than that in bulk system. A large variety of solid and liquid structures are observed for water confined in slit [3, 4] and cylindrical [5] pores. For dynamical properties, the mean square displacement of confined liquids behaves in a different way from the diffusion law in bulk liquids [6]. This section is devoted to review several topics in phase behavior of confined materials, specifically for freezing behavior.

Confining material

According to the International Union of Pure and Applied Chemistry (IUPAC), microporous materials are defined as porous materials with pore diameter less than 2 nm, mesoporous materials are defined as those with pore diameter between 2 and 50 nm, and macroporous materials are defined as those with pore diameter larger than 50 nm [7]. One of the most famous porous materials in the experimental study of confined fluids is porous silica glasses. Their pore structures are characterized by a complex network of tubule pores. Vycor glass has small pore size distribution (e.g., $40\text{\AA} \pm 5\text{\AA}$) and the pore surface is hydrophilic [8]. Pore materials with simple and regular geometry are also available. The cylindrical pores in MCM-41 [9] and carbon nanotubes [10] are close to the regular cylinder. MCM-41 has a hexagonal ordered array of cylindrical pores with diameters varying from 1 to 10 nm [11]. On the other hand, a carbon nanotube has a single cylindrical pore in its hollow cylindrical shape. Also, the surface of a carbon nanotube is chemically inert. These materials are used in experiment to investigate physical properties of fluids in cylindrical pores. Slit pores with pore size around 1 nm are found in activated carbon fibre and pillared clay [11]. However, the pores in these materials are disordered. Porous materials with ordered slit pores are less available compared to ordered cylindrical pores. Instead, fluids confined in a simple slit pore geometry can be investigated with the aid of surface force apparatus (SFA).

Experimental methods for confined fluids

Neutron scattering

Using small angle neutron scattering, the density of confined fluids can be measured from the intensity of the Bragg peak for regular cylindrical pore [11]. On the other hand, wide angle neutron scattering, which is a major tool to investigate the local structure in condensed matters, serves as a tool of direct detection of phase transition in confined fluids [11].

Surface force apparatus (SFA)

This method [11–13] is specific to the study of slit pore. The sample is confined between two planer walls by capillary condensation. Mica is often used for the confining wall since it has smooth surface and is chemically inert. The surface separation H can be varied in accuracy of 0.1 nm. Both the normal force and the lateral shear force exerted on the walls can be measured as

a function of H . If there is a layering structure, it is observed as oscillation in the normal force profile. On the other hand, the phase transition is detected as a sudden change in the lateral shear force profile.

Dielectric spectroscopy

This method can be used to detect solid-liquid phase transitions of polar fluids via temperature dependence of the real part of the relative permittivity. Measurement of dielectric relaxation time is used to obtain structural information, such as the existence of contact layer at the pore wall. It is known that such liquid layer of polar molecules exhibits low relaxation time of the order of 10^{-6} s [14].

Differential Scanning Calorimetry (DSC)

In principle, this method can be used to study any events that are accompanied by the heat exchange between the sample material and surroundings. For the study of materials confined in pores, this method is widely used to determine the shift of transition temperature from bulk values or explore the existence of new stable or metastable phases, etc. However, as the pore size decreases, the determination of the freezing temperature becomes more difficult since the peak in the DSC signal corresponding to the transition becomes broader. The temperature is varied at about 1-10 K/min [11, 15].

Shift of freezing temperature due to confinement

The spacial restriction affects the freezing temperature of a material. In earlier studies [16–18] on fluids confined in silica nanoporous materials, two features are commonly observed. First, the freezing temperature in the pore is lower than bulk freezing temperature. Second, the smaller the pore size, the larger the lowering of the freezing temperature. From these results, it was once believed that freezing temperature is always lowered by confinement. However, experimental study on a fluid confined in a slit pore between two mica surfaces by surface force apparatus (SFA) revealed that the freezing temperature is elevated in the pore [12]. Also, it is shown by molecular simulation that Lennard-Jones methane molecules confined in a slit [19] or cylindrical [20] pore exhibit the freezing temperature depression for hard-walls, while it exhibits higher freezing tem-

perature for as strong an attractive wall as graphite. In this way, the direction of the shift of melting temperature in pore is sensitive to the nature of fluid-wall interaction. More precisely, the ratio of the strength of fluid-wall attraction to that of fluid-fluid attraction determines the magnitude and direction of the shift of freezing temperature. As this ratio is smaller, the freezing temperature tends to be lowered. For fluids with moderate attractive interaction, this ratio is small for nanoporous silica, while it is large for mica or graphite. The fluid-wall interaction also affects the liquid-vapor transition temperature of confined fluids. For water between two planer walls, effects of the wall-fluid interaction on capillary evaporation or condensation at fixed temperature (300 K) are examined by simulation for pressures $-0.15 \text{ GPa} \leq P \leq 0.2 \text{ GPa}$ and pore width $0.4 \text{ nm} \leq H \leq 1.6 \text{ nm}$ [21]. When the plates are hydrophobic, capillary evaporation is observed. On the other hand, capillary condensation is observed for hydrophilic plates at all P and H studied.

For larger pores with regular geometry, the shift in freezing point due to confinement is well described by Gibbs-Thomson equation:

$$\Delta T_f = T_f^{\text{bulk}} - T_f^{\text{pore}} = \frac{A}{V} \frac{T_f^{\text{bulk}} \nu (\gamma_{\text{ws}} - \gamma_{\text{wl}})}{\Delta H_m}, \quad (1)$$

where, T_f^{pore} and T_f^{bulk} is the freezing temperature in the pore and in bulk, respectively, γ_{ws} and γ_{wl} the substrate-solid and substrate-liquid surface tensions, respectively, ΔH_m the melting enthalpy, and ν the molar volume (the difference in the molar volume between solid and liquid phases is neglected). A/V is the ratio of the total area of confining surface to the total volume of the pore space: for slit pores between two identical plates with the separation distance H , $A/V = 2/H$; for cylindrical pore with the diameter D , $A/V = 4/D$. The direction of temperature shift depends on the sign of $\gamma_{\text{ws}} - \gamma_{\text{wl}}$. According to Eq. (1), the freezing temperature is lowered when the surface of the confining wall favors liquid phase. This equation indicates that the magnitude of the freezing temperature shift is proportional to the inverse of the pore size.

Since Gibbs-Thomson equation is based on the thermodynamics of macroscopic systems, there is no reason that it is valid for pore sizes as small as several molecular diameters. Also, for the pore sizes of the order of several molecular diameters, the macroscopically defined surface tension [γ_{ws} and γ_{wl} in Eq. (1)] does not make sense. Actually, the study of dielectric spectroscopy measurement for nitrobenzene confined in controlled pore glasses revealed that the linear dependence of ΔT_f on

the inverse of the pore diameter is observed for pore diameters larger than 4.0 nm, while ΔT_f for smaller diameters deviates from the linearity [14]. On the other hand, experimental study of water confined in the cylindrical pores of MCM-41 showed that the shift of the freezing point is in good agreement with Gibbs-Thomson equation, provided that the thickness of the ‘bound water’ is subtracted from the pore radius [22]. Bound water is a fluid-like layer between the inner ice and confining surface, which is widely observed in experiment [23].

Continuous freezing in confined liquids

Another remarkable aspect of the freezing in confined fluids is that the freezing may occur as a continuous phase change. From the thermodynamic viewpoint, this means that there is no discontinuity in the first derivative of molar free energy with a field variable, such as number density of adsorbed molecules. Such behavior is analogous to the continuous isotherms above the gas-liquid critical point on the pressure–density plane. However, the freezing in bulk fluids is always accompanied by a discontinuous change in order parameters.

To obtain a basic knowledge of phase behavior of confined fluids, it is important to consider a simple and regular confining geometry with smooth surfaces. The examples are a slit pore between two identical parallel plates with a surface area A and a separation distance H and a tubule pore inside a hollow cylinder with an axial length L and a pore diameter D . The problem is more simplified if the dimensions parallel to the confining wall are taken to be infinity: $A \rightarrow \infty$ for the slit pore and $L \rightarrow \infty$ for the cylindrical pore. This leads to a quasi two-dimensional system of width H for the slit pore, and a quasi one-dimensional system with diameter D for the cylindrical pore. Therefore, the geometry of each pore is completely specified by single parameter, H or D . In experiment, single-walled carbon nanotubes are used to investigate quasi one-dimensional systems since their aspect ratio (axial length/diameter) is sufficiently large ($\sim 10^4$); MCM-41 has relatively small values ($\sim 10^2 - 10^3$). Materials with an ideal slit pore are less available. Instead, one can deal with ideal slit pores by using the surface force apparatus. For simulation studies, the finite-size limitation of simulation box is less serious, especially for quasi one-dimensional systems, where the system size is proportional to the cell length.

There are vast studies on the effect of pore size on freezing behavior using pore materials with regular geometry. Experimental methods, such as X-ray diffraction, NMR, and dielectric

spectroscopy, are used to examine the freezing behavior in confined fluids. In both experiment and simulation, it is observed that for fluids confined in cylindrical pores with diameters on nanometer scale, the sharpness of continuous phase change is strongly dependent on the pore diameter D , and that freezing becomes always more gradual as D decreases.

Lattice model

In theoretical approach, simple lattice models are proved to be able to capture the essential effect of the dimensionality on phase behavior. An example is the Ising model [24] in which it is assumed that a molecule fixed at each lattice point can be in either one of two different states, and that only neighboring molecules interact with each other. Although such treatment seems to be too simplified, it may exhibit gas-liquid phase transition and critical point. When the dimensionality of the lattice is less than two, the Ising model never exhibits the first-order phase transition since the partition function has an analytical form, i.e., there cannot be any singularity in thermodynamic properties. However, it is rigorously proved that the two-dimensional Ising model exhibits a finite critical point temperature [25].

Lattice models can be used to study the effect of pore size on the sharpness of phase change. This problem is extensively studied by the finite-size scaling method under the title of “rounding” of the first order transition [26, 27]. In the finite-size scaling approach, an order parameter ρ as a function of a thermodynamic variable x is expressed in such a form

$$\rho = f\left(\frac{x}{s(D)}\right), \quad (2)$$

where D is a characteristic variable of the finite size of the system [for an infinitely long cylindrical lattice, for example, the number of lattice points perpendicular to the cylindrical axis (see Fig. 1)]. The speed at which ρ varies with x is governed by $s(D)$. The smaller the magnitude of $s(D)$, the sharper the variation of ρ with x becomes. When $s(D)$ is a rapidly decreasing function, the sharpness of $\rho(x)$ increases rapidly as D increases. In Fig. 2, a comparison is made for the model function $\rho(x) = \tanh[x/s(D)]$ between two choices of $s(D)$.

For ferromagnetic Ising model of the infinitely long cylindrical lattice, the variation of the magnetization per spin m with changing the external field h at fixed temperature T has the form [26]

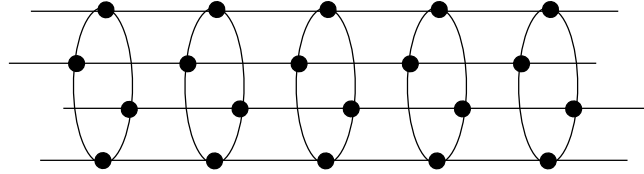


Figure 1: Infinitely long cylindrical lattice with finite width $D = 4$.

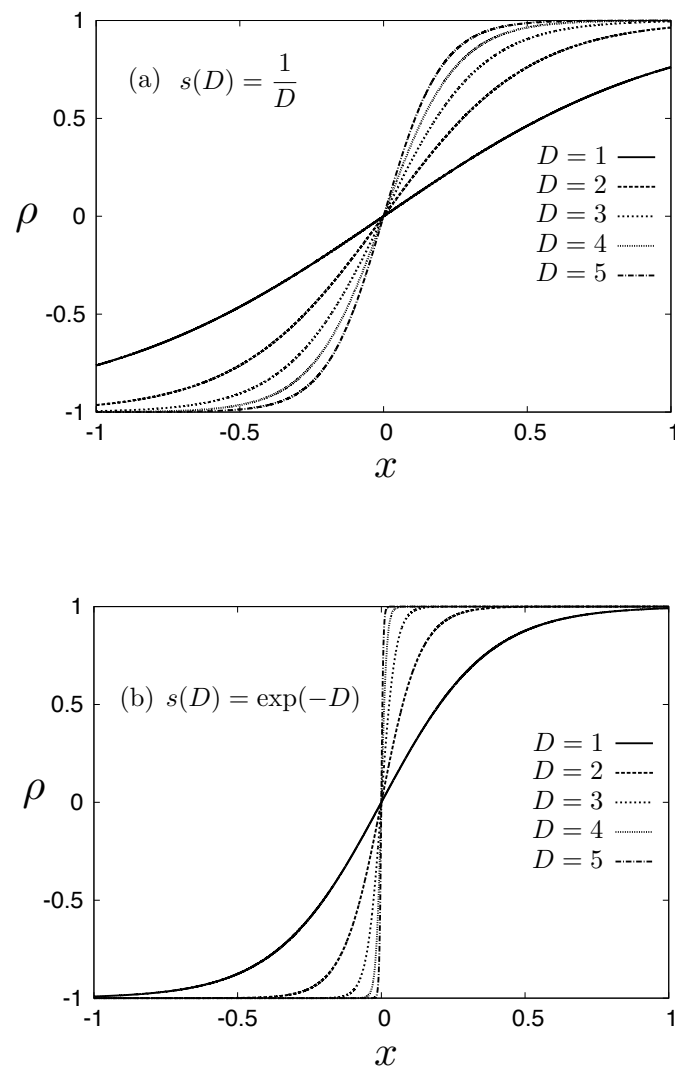


Figure 2: Demonstration of the effect of increasing D on the sharpness of a model function $\rho(x) = f[x/s(D)] = \tanh[x/s(D)]$ for (a) $s(D) = 1/D$ and (b) $s(D) = \exp(-D)$.

$$m(h; D) \sim m_0 f\left[\frac{h}{s(D)}\right], \quad (3)$$

here m_0 is the spontaneous magnetization in the two-dimensional limit ($D \rightarrow \infty$), and

$$s(D) = \frac{m_0}{kT} D \exp\left(-\frac{\sigma D}{kT}\right) \sim \exp\left(-\frac{\sigma D}{kT}\right), \quad (4)$$

where σ is the interfacial tension between the domains of up-spin and down-spin states. It is pointed out in [26] that to derive the exponential form, the effect of the interfacial tension has to be taken into account.

For the capillary condensation in the lattice gas model with cylindrical geometry, a crude estimation, $\mu - \mu_{\text{sat}} \sim \exp[-(D/\sigma)^2]$, is proposed for the sharpness of the adsorption–chemical potential curve, where μ is the chemical potential of the system, μ_{sat} is the chemical potential at which the bulk coexistence occurs, and σ is molecular diameter [28].

Statistical mechanics of solvation

Fundamentals and excess chemical potential

Consider a binary solution composed of solute species A and solvent species B. The numbers N_A, N_B of the two species and the volume V are assumed to be macroscopically large. The chemical potential μ_A of the solute at temperature T is expressed by the change in the Helmholtz free energy by adding a solute molecule to the original system with N_B, T, V fixed

$$\mu_A = A_{(N_A+1)} - A_{(N_A)}. \quad (5)$$

The free energy A is a function of N_A, N_B, V , and T . Eq.(5) is a definition of chemical potential in thermodynamics. The goal here is to show, by using the framework of statistical mechanics, that μ_A can be divided into two parts; one comes from ideal gas behavior and the other comes from intermolecular interactions.

Statistical mechanics provides the connection between Helmholtz free energy and the partition function Z :

$$A = -kT \ln Z. \quad (6)$$

For the present case, Z is a function of N_A , N_B , V , and T . If the system is composed of classical monatomic molecules,

$$Z = \frac{Q_{N_A, N_B}}{N_A! \Lambda_A^{3N_A} N_B! \Lambda_B^{3N_B}}, \quad (7)$$

where Λ_A and Λ_B are the de Broglie wave length of each species and depend on T but not on the extensive variables N_A , N_B , and V . Q_{N_A, N_B} is called the configuration integral and is the integral of a Boltzmann factor over all possible positions of solvent and solute molecules in the volume V :

$$\int_V \dots \int_V \exp(-U_{N_A, N_B}/kT) d\mathbf{r}^{N_A} d\mathbf{r}^{N_B}, \quad (8)$$

where, k is Boltzmann's constant and U_{N_A, N_B} is the total potential energy due to the intermolecular interaction. The abbreviation $d\mathbf{r}^{N_A} = d\mathbf{r}_{A,1} d\mathbf{r}_{A,2} \dots d\mathbf{r}_{A,N_A}$ is used with $\mathbf{r}_{A,i}$ being the positional vector of the i th solute molecule, and similarly $d\mathbf{r}^{N_B} = d\mathbf{r}_{B,1} d\mathbf{r}_{B,2} \dots d\mathbf{r}_{B,N_B}$ for solvent molecules. The nature of species is reflected in the de Broglie wave length and configuration integral. The former is determined by intramolecular properties while the latter is determined by intermolecular potentials. Using Eqs. (6), (7), and (8), Eq. (5) is rewritten as

$$\mu_A = kT \ln N_A \Lambda_A^3 + kT \ln \frac{Q_{N_A, N_B}}{Q_{N_A+1, N_B}}, \quad (9)$$

where, Q_{N_A+1, N_B} is the configuration integral for the system composed of $N_A + 1$ solute molecules and N_B solvent molecules. Let us rewrite Q_{N_A+1, N_B} as follows,

$$\begin{aligned} Q_{N_A+1, N_B} &= \int_V \dots \int_V \exp(-U_{N_A+1, N_B}/kT) d\mathbf{r}^{N_A+1} d\mathbf{r}^{N_B}, \\ &= \int_V \left[\int_V \dots \int_V \exp(-U_{N_A+1, N_B}/kT) d\mathbf{q}^{N_A} d\mathbf{q}^{N_B} \right] d\mathbf{r}. \end{aligned} \quad (10)$$

In the second line, a set of new coordinations are used,

$$\begin{aligned}
\mathbf{q}_{A,1} &= \mathbf{r}_{A,1} - \mathbf{r}, \\
&\vdots \\
\mathbf{q}_{A,N_A} &= \mathbf{r}_{A,N_A} - \mathbf{r}, \\
\mathbf{q}_{A,N_A+1} &= \mathbf{r}, \\
\mathbf{q}_{B,1} &= \mathbf{r}_{B,1} - \mathbf{r}, \\
&\vdots \\
\mathbf{q}_{B,N_B} &= \mathbf{r}_{B,N_B} - \mathbf{r},
\end{aligned} \tag{11}$$

where $\mathbf{r} \equiv \mathbf{r}_{A,N_A+1}$ is the positional vector of the $(N_A + 1)$ th solute molecule. Since the total intermolecular potential energy U_{N_A+1,N_B} is determined by the mutual positions of the $N_A + 1 + N_B$ molecules ($\mathbf{q}_{A,1}, \dots, \mathbf{q}_{A,N_A}$ and $\mathbf{q}_{B,1}, \dots, \mathbf{q}_{B,N_B}$), the integrand is independent of the position \mathbf{r} . Hence, integration over \mathbf{r} can be carried out, yielding a multiplying factor V :

$$Q_{N_A+1,N_B} = V \int_V \dots \int_V \exp(-U_{N_A+1,N_B}/kT) d\mathbf{q}^{N_A} d\mathbf{q}^{N_B} \equiv V Q_{N_A,N_B}^{(1)}(\mathbf{r}). \tag{12}$$

The corresponding system of the configuration integral $Q_{N_A,N_B}^{(1)}(\mathbf{r})$ is that one additional solute molecule is fixed at the position \mathbf{r} in the system of N_A solute and N_B solvent molecules. Note that this additional solute molecule does not need to be the $(N_A + 1)$ th solute molecule since all N_A solute molecules are identical.

Finally, the chemical potential of the solute is expressed by

$$\mu_A = kT \ln \rho_A \Lambda_A^3 + kT \ln \frac{Q_{N_A,N_B}}{Q_{N_A,N_B}^{(1)}(\mathbf{r})}, \tag{13}$$

where $\rho_A = N_A/V$ is the number density of the solute. If there were no intermolecular interaction, the second term would vanish since $Q_{N_A,N_B} = Q_{N_A,N_B}^{(1)}(\mathbf{r}) = V^{N_A+N_B}$. Therefore, the first term

$$\mu_{id} \equiv kT \ln \rho_A \Lambda_A^3, \tag{14}$$

is identified as the chemical potential of the species A if it behaves as the ideal gas. The residual

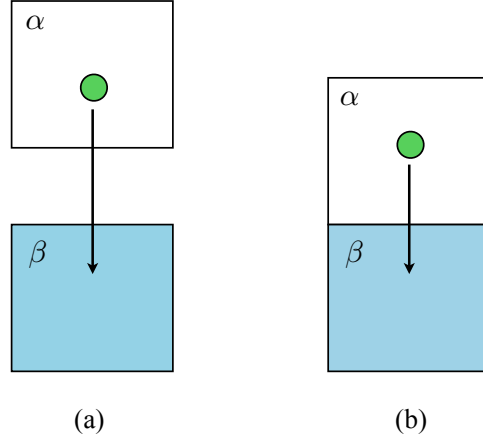


Figure 3: Schematic image of transfer of one solute molecule from the phase α to the phase β . In (a), the transfer is carried out for the two phases that are not in equilibrium, while (b) illustrates the special case that the two phases are in equilibrium, and therefore have the same chemical potential and temperature.

part

$$\mu_{\text{ex}} \equiv \mu_A - \mu_{\text{id}} = -kT \ln \frac{Q_{N_A, N_B}^{(1)}(\mathbf{r})}{Q_{N_A, N_B}}, \quad (15)$$

is called excess chemical potential, since all effect of intermolecular interaction is involved in this term. The second equality in Eq. (15) is important since it serves as the common starting point for the derivation of different methods of calculating μ_{ex} .

Excess chemical potential and Ostwald adsorption coefficient

Let us imagine that there are two phases α and β containing solute molecules of species A and consider such a process that one solute molecule in the phase α is transferred to the phase β . The two phases need not to be at the same temperature or chemical potential of the solute. The free energy change during this process is equal to the difference of the chemical potential of the solute in phase α and phase β , $\mu_A^\beta - \mu_A^\alpha$. Note that this is correct even when the two phases are not in equilibrium with each other (Fig. 3a). As a special case, when the phases α and β are in equilibrium (Fig. 3b), like the liquid-gas coexistence, the temperature is common for the two phases and so is the chemical potential of the solute ($\mu_A^\alpha = \mu_A^\beta$). Hence, from the definition of μ_{ex} in Eq. (15) and the

expression of μ_{id} [Eq. (14)],

$$\mu_{\text{ex}}^{\beta} - \mu_{\text{ex}}^{\alpha} = \mu_{\text{id}}^{\alpha} - \mu_{\text{id}}^{\beta} = -kT \ln \frac{\rho_{\text{A}}^{\beta}}{\rho_{\text{A}}^{\alpha}}. \quad (16)$$

On the right-hand side, the contributions from de Broglie wave length cancel due to the common temperature. Now let α and β be gas and liquid phases, respectively, and assume that they are in equilibrium. When the solute is very dilute in the gas phase, it can be regarded as the ideal gas ($\mu_{\text{ex}}^{\alpha} \simeq 0$), and therefore

$$\mu_{\text{ex}}^{\beta} = -kT \ln \frac{\rho_{\text{A}}^{\beta}}{\rho_{\text{A}}^{\alpha}}. \quad (17)$$

Eq. (17) indicates that the excess chemical potential in the liquid phase can be determined from $\rho_{\text{A}}^{\alpha}/\rho_{\text{A}}^{\beta}$. This ratio is called Ostwald absorption coefficient. In experiments, gas solubility data in acceptable accuracy were already available in 1900s [29] and there are a vast number of reports on the measurement of Ostwald coefficient of various gaseous solute molecules [30–35].

Theoretical methods to calculate μ_{ex}

In theoretical approach, an important task is to determine the solvation free energy for a given intermolecular interaction, on the basis of statistical methanics. Such knowledge cannot be obtained by the discussion in the previous subsection, where no information on intermolecular interaction was referred to. In what follows, two well-known methods (test particle method [36] and thermodynamic integration method [37]) for the calculation of μ_{ex} for a given intermolecular potential are derived from Eq. (15). These methods provide recipes to calculate μ_{ex} by using molecular simulation. For this purpose, it is convenient to introduce a function Φ by

$$\Phi = U_{N_{\text{A}}+1, N_{\text{B}}} - U_{N_{\text{A}}, N_{\text{B}}}. \quad (18)$$

This is the potential energy change when a solute molecule is added at a fixed point in the system of N_{A} solute molecules and N_{B} solvent molecules, with the positions of all the $N_{\text{A}} + N_{\text{B}}$ molecules being fixed. For many cases, this energy difference can be expressed as the sum of pair interactions of the added solute molecule with all the other molecules.

Thermodynamic integration method

Let us define a function

$$Q(\lambda) = \int_V \dots \int_V \exp[-[f(\lambda)\Phi + U_{N_A, N_B}]/kT] \mathbf{d}\mathbf{r}^{N_A} \mathbf{d}\mathbf{r}^{N_B}, \quad (19)$$

where $f(\lambda)$ is an arbitrary continuous function such that $f(\lambda = 0) = 0$ and $f(\lambda = 1) = 1$. Eq. (15) can be rewritten as

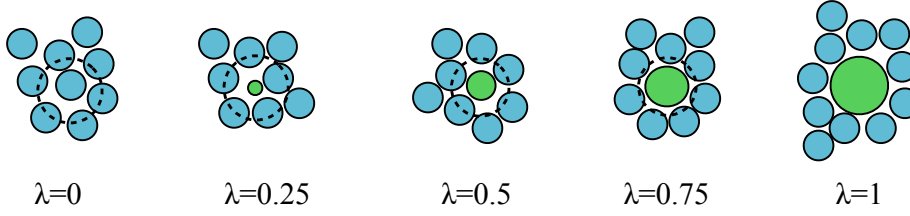
$$\begin{aligned} \mu_{\text{ex}} &= -kT \ln \frac{Q(\lambda = 1)}{Q(\lambda = 0)} \\ &= -kT \int_0^1 \frac{d \ln Q(\lambda)}{d\lambda} d\lambda \\ &= \int_0^1 f'(\lambda) \left(\int_V \dots \int_V \Phi \frac{\exp\{-[f(\lambda)\Phi + U_{N_A, N_B}]/kT\}}{Q(\lambda)} \mathbf{d}\mathbf{r}^{N_A} \mathbf{d}\mathbf{r}^{N_B} \right) d\lambda, \end{aligned} \quad (20)$$

where $f'(\lambda)$ is the derivative of $f(\lambda)$. The part (\dots) in the third line can be regarded as taking average of the quantity Φ over such ensemble that the added solute molecule interacts with solvent molecules through the modified potential $f(\lambda)\Phi$. If this average is denoted by $\langle \Phi \rangle_\lambda$, Eq. (20) is expressed by

$$\mu_{\text{ex}} = \int_0^1 f'(\lambda) \langle \Phi \rangle_\lambda d\lambda. \quad (21)$$

This is a final expression of thermodynamic integration method. Usually, $\langle \Phi \rangle_\lambda$ for several values of λ are calculated by performing different simulations for each value of λ . The obtained data are fitted by a polynomial so that the integration in Eq. (21) can be carried out. The form $f(\lambda) = \lambda^n$ is often used. In this case, going from $\lambda = 0$ to $\lambda = 1$ corresponds to a reversible process of gradually “switching on” the interaction between the added solute molecule and all solvent molecules (Fig. 4a). It should be noted that when moving from the first to the second line in Eq. (20), it was tacitly assumed that the function $Q(\lambda)$ (and the corresponding Helmholtz free energy) be differentiable with respect to λ at any $0 \leq \lambda \leq 1$. This condition breaks down if there occurs a phase transition during changing λ , which results in a discontinuity in the chemical potential.

(a) Thermodynamic integration



(b) Test particle

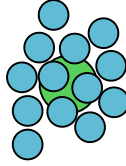


Figure 4: Relevant ensembles for the two methods of calculating μ_{ex} . In the thermodynamic integration method (a), the solute molecule gradually emerges from no existence ($\lambda = 0$) to complete existence ($\lambda = 1$). In the test particle method (b), the solvent molecules do not feel the existence of the solute molecule [therefore, the same ensemble as that with $\lambda = 0$ in (a)]. Solvent is blue and solute green.

Test particle method

Let us rewrite Eq. (15) by using Eq. (18) as

$$\begin{aligned}
 \mu_{\text{ex}} &= \int_V \dots \int_V \exp(-\Phi/kT) \frac{\exp(-U_{N_A, N_B}/kT)}{\mathcal{Q}_{N_A, N_B}} d\mathbf{r}^{N_A} d\mathbf{r}^{N_B} \\
 &= \langle \exp(-\Phi/kT) \rangle_{N_A, N_B}.
 \end{aligned} \tag{22}$$

The first line means taking average value of the quantity $\exp(-\Phi/kT)$ in such ensemble that only N_A solute molecules and N_B solvent molecules are present in the system (the same ensemble as that with $\lambda = 0$ in thermodynamic integration method). In the second line, this averaging is denoted by $\langle \dots \rangle_{N_A, N_B}$. The average quantity can be calculated if we imagine that the additional solute molecule is fixed at a position \mathbf{r} but behaves like a “ghost”, and monitor the value of $\exp(-\Phi/kT)$ as the other $N_A + N_B$ molecules are moving around. The N_A solute and N_B solvent molecules may overlap

with the added particle, since they don't feel the existence of it (Fig. 4b). When they overlap, Φ has a large positive value due to the strong repulsion of atomic cores, and therefore the value of $\exp(-\Phi/kT)$ becomes almost zero. If there is no overlap, on the other hand, the value has positive values due to the attractive interaction between the solute and solvent molecules. The magnitude of Φ depends on the number of other molecules that are close to the additional solute molecule. If the system is homogeneous, the average quantities calculated at different r must be the same.

An advantage of the test particle method compared to the thermodynamic integration method is that simulation of one system is sufficient. Also, when one wishes to calculate μ_{ex} of another different molecule, additional simulation is not needed as long as the thermodynamic condition of the solution is the same and the new solute is infinitely dilute. However, use of this method is impractical when the size of solute is too large or the total density of the solution is too high, since the trial insertion almost always fails. In such cases, the thermodynamic integration method serves as a complementary method.

Infinite dilution

For some cases, the solubility (more precisely, the mole fraction of the solute) in a solution is very low. A typical example is the low solubility of hydrophobic molecules in water (the mole fraction is $\sim 1/1000$). The lower the solubility, the more rarely a solute molecule finds other solute molecules. Therefore, for sufficiently dilute solutions, it is expected that the solvation properties of single solute molecule are essentially the same as those of the solution that contains only one solute molecule. This is the motivation of introducing the condition of infinite dilution, $N_A/V \rightarrow 0$, which has meaning in the thermodynamic limit: $N_A \rightarrow \infty, V \rightarrow \infty$. With this condition, the simulation of a pure solvent is enough for the calculation of the excess chemical potential of solute with the test particle method. Infinite dilution condition can be considered for inhomogeneous system, too, as far as there is no large density fluctuation at any part of the entire volume V .

Solvation at liquid-vapor interface

Structure of liquid-vapor interface

Macroscopically, the interface between liquid and solid phases looks like a boundary plane between

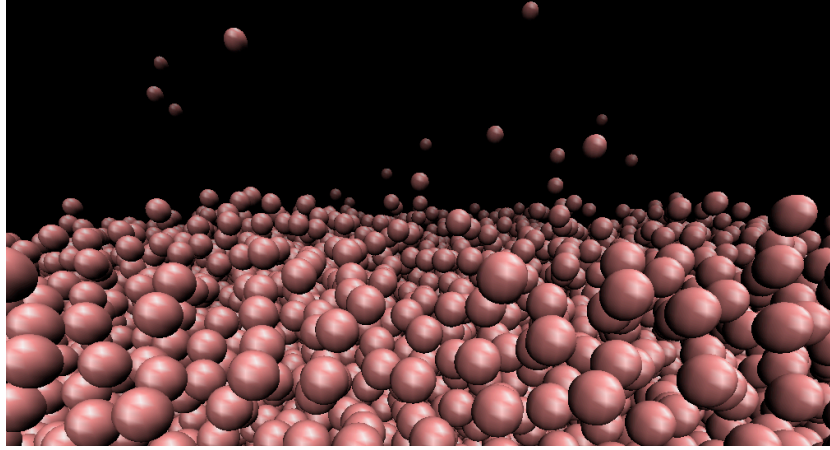


Figure 5: Microscopic view of the liquid-vapor interface: a snapshot from a molecular dynamics simulation of a Lennard-Jones fluid. The gas phase is on the upper side, while the liquid phase is on the lower side.

the two phases. However, in a microscopic view, there is no such a definite plane. Instead, there is a very thin inhomogeneous region which is neither gas nor liquid phases (see Fig.5). It is clear that there is no unique way of defining the interface as a single plane. For the interface of water near the triple point temperature, the thickness of the interface is about 2 nm.

Local excess chemical potential

In the liquid-vapor interface, the local density ρ_A of solute molecules is dependent on the position. For a planar liquid-vapor interface, ρ_A depends only on the interface-normal axis z . As shall be derived in Chapter 2 and 3, the ratio of the local solute density $\rho_A(z)$ to the activity of the solute ζ_A is expressed as,

$$\frac{\rho_A(z)}{\zeta_A} = \langle \exp[-\Phi(z)/kT] \rangle. \quad (23)$$

This is the extension of test particle theory to a system that is inhomogeneous along only one direction. At infinite dilution ($\rho_A \rightarrow 0$), ζ_A can be replaced by the solute density in the coexisting gas phase, ρ_A^g . Therefore,

$$\frac{\rho_A(z)}{\rho_A^g} = \langle \exp[-\Phi(z)/kT] \rangle \equiv \Sigma(z). \quad (24)$$

The quantity $\rho_A(z)/\rho_A^g \equiv \Sigma(z)$ is a similar form to the Ostwald adsorption coefficient. The local excess chemical potential can be introduced by

$$\mu_{\text{ex}}(z) = -kT \ln \Sigma(z). \quad (25)$$

Outline of the present study

In the following three chapters, simulation studies on the two types of inhomogeneous fluids are presented: confined fluids and liquid-vapor interface. For the former, the topic to be dealt with is continuous freezing in a cylindrical pore, and for the latter, solubility of hydrophobic molecules in the liquid-vapor interface of water.

In Chapter 1, freezing behavior of a liquid monolayer adsorbed in a nanoscale cylindrical pore, like that found in a single-walled carbon nanotube, is studied. The single-layer structure can be formed at sufficiently low pressures (or sufficiently low chemical potentials) of the reservoir. The liquid monolayer is described by a quasi one-dimensional lattice model with nearest-neighbor interaction. This model can be mapped to the Ising model, which means that any thermodynamic properties of the model monolayer can be derived from those of Ising model. The main purpose is to clarify the effect of varying the pore diameter on the sharpness of freezing. The experimentally observed rapid change in the sharpness by increasing pore diameter is observed for the present model. The model also predicts that a stable, partially-frozen state occurs between solid and liquid phases if the pair interaction of fluid molecules has a certain anisotropy.

Chapters 2 and 3 deal with the solubility of small, spherical, and nonpolar molecules in the liquid-vapor interface of water. The quantity to be obtained is the local excess chemical potential $\mu_{\text{ex}}(z)$, where z is the coordinate perpendicular to the interface. More precisely, the main property to be discussed is the local quantity $\Sigma(z) = \exp(-\mu_{\text{ex}}(z)/kT)$, which will be termed as local solubility. The local solubility is calculated by molecular dynamics simulation combined with test particle method. All results are compared with those for the interface of a simple liquid. In Chapter 2, effects of the strength of solute-solvent attraction on the local solubility are investigated at a fixed temperature near the triple point. A stepwise analysis is performed to identify the key factor responsible for the resulting lower values of local solubility in the interface of water compared to the

interfaces of simple liquids. It is shown that the key factor is the water's higher value of the triple point temperature, and that the interfacial structure of water has a higher ability to dissolve the solute molecule than those of simple liquids. Finally, the probability of cavity formation is calculated in order to account for the difference in the dissolution ability of the two solvents.

In Chapter 3, temperature effects on the local solubility are examined for methane in the liquid-vapor interface of water and of krypton. Additionally, a model system of Lennard-Jones (LJ) particles in the interface of a LJ fluid is considered. The model system is chosen so as to exhibit qualitatively the same temperature dependence of solubility as that found for bulk aqueous solutions of hydrophobic molecules. The local solubility is obtained for various temperatures near the triple point, including supercooled region. As shall be seen, the model system takes an important role in determining the properties of local solubility that are specific to the interface of water. The analysis is two-fold. First, the shape of $\Sigma(z)$ and its temperature dependence are examined. For methane in water, previously reported features of $\mu_{\text{ex}}(z)$, such as the minimum (interface adsorption) and maximum (free energy barrier), are observed. It is found that the maximum in $\mu_{\text{ex}}(z)$ is explained by the interfacial structure of water. Second, the temperature dependence of Σ is examined at different conditions: fixed position z and fixed solvent density. This is the extension of the fixed-pressure and fixed-volume conditions in bulk solutions to the liquid-vapor interface. The fixed-density condition in the interfacial system is realized by introducing a coarse-grained solvent density. It is found that the effects of fixing z or fixing density on the temperature dependence of the local solubility in the interfacial systems are very similar to those of fixing pressure or fixing volume on the temperature dependence of the solubility in bulk solutions, respectively. Especially, all the three systems exhibit a monotonic decrease of the local solubility with temperature, at *any* fixed solvent densities between those in gas and liquid phases. Monotonic decrease of the solubility with temperature at fixed volume is already confirmed for bulk solutions of nonpolar molecules both in water and in simple liquids.

Finally, the conclusions of the present study are summarized.

References

- [1] S. Nosé. *J. Chem. Phys.*, **81**, 511 (1984).

- [2] S. Nosé. *Mol. Phys.*, **52**, 255 (1984).
- [3] N. Kastelowitz, J. C. Johnston, and V. Molinero. *J. Chem. Phys.*, **132**, 124511 (2010).
- [4] S. Han, M. Y. Choi, P. Kumar, and H. E. Stanley. *Nat. Phys.*, **6**, 685 (2010).
- [5] K. Koga, G. Gao, H. Tanaka, , and X. Zeng. *Nature*, **412**, 802 (2001).
- [6] Y.-C. Liu, J. D. Moore, T. J. Rousselzb, and K. E. Gubbins. *Phys. Chem. Chem. Phys.*, **12**, 6632 (2010).
- [7] *IUPAC Manual of Symbols and Terminology, Appendix 2.*, volume 31, page 578 (1972).
- [8] F. Bruni, M. A. Ricci, and A. K. Soper. *J. Chem. Phys.*, **109**, 1478 (1998).
- [9] J. S. Beck, J. C. VartUli, W. J. Roth, M. E. Leonowicz, C. T. Kresge, K. D. Schmitt, C. T.-W. Chu, D. H. Olson, E. W. Sheppard, S. B. McCullen, J. B. Higgins, and J. L. Schlenker. *J. Am. Chem. Soc.*, **114**, 10834 (1992).
- [10] S. Iijima. *Nature*, **354**, 56 (1991).
- [11] C. Alba-Simionesco, B. Coasne, G. Dosseh, G. Dudziak, K. Gubbins, R. Radhakrishnan, , and M. Sliwinska-Bartkowiak. *J. Phys. Condens. Matter*, **18**, R15 (2006).
- [12] J. N. Israelachivili, P. M. McGuiggan, and A. M. Homola. *Science*, **240**, 189 (1988).
- [13] H. K. Christenson. *J. Phys. Condens. Matter*, **13**, R95 (2001).
- [14] M. Sliwinska-Bartkowiak, J. Gras, R. Sikorski, R. Radhakrishnan, L. Gelb, and K. E. Gubbins. *Langmuir*, **15**, 6060 (1999).
- [15] G. Dosseh, Y. Xia, and C. Alba-Simionesco. *J. Phys. Chem. B*, **107**, 6445 (2003).
- [16] L. D. Gelb, K. E. Gubbins, R. Radhakrishnan, and M. Sliwinska-Bartkowiak. *Rep. Prog. Phys.*, **62**, 1573.
- [17] H. F. Booth and J. H. Strange. *Mol. Phys.*, **93**, 263.
- [18] E. W. H. R. Schmidt, M. Stocker, and D. Akporiaye. *J. Phys. Chem.*, **99**, 4148 (1995).

- [19] M. Miyahara and K. E. Gubbins. *J. Chem. Phys.*, **106**, 2865 (1997).
- [20] M. Maddox and K. E. Gubbins. *J. Chem. Phys.*, **107**, 9659 (1997).
- [21] N. Giovambattista, P. J. Rossky, and P. G. Debenedetti. *Phys. Rev. E*, **73**, 041604 (2006).
- [22] K. Morishige and K. Kawano. *J. Chem. Phys.*, **110**, 4867 (1999).
- [23] K. Overloop and L. V. Gerven. *Magn. Reson. A*, **101**, 179 (1993).
- [24] E. Ising. *Z. Phys.*, **31**, 253 (1925).
- [25] L. Onsager. *Phys. Rev.*, **65**, 117 (1944).
- [26] V. Privman and M. E. Fisher. *J. Stat. Phys.*, **33**, 385 (1983).
- [27] M. E. Fisher and A. N. Berker. *Phys. Rev. B*, **26**, 2507 (1982).
- [28] R. Evans. Liquids at interfaces. In J. Charvolin, J. Joanny, and J. Zinn-Justin, editors, *Les Houches Session XLVIII*. Elsevier, Amsterdam (1990).
- [29] E. Wilhelm. *CRC Crit. Rev. Analyt. Chem.*, **16**, 129 (1985).
- [30] A. Ben-Naim and J. Wilf. *J. Sol. Chem.*, **12**, 861 (1983).
- [31] A. Ben-Naim and R. Battino. *J. Sol. Chem.*, **14**, 245 (1985).
- [32] T. J. Morrison and F. Billett. *J. Chem. Soc.*, , 3819 (1952).
- [33] W. Prapaitrakul and A. D. King, Jr. *J. Colloid Interface Sci.*, **112**, 387 (1986).
- [34] W. Wen-Yang and J. H. Hung. *J. Phys. Chem.*, **74**, 170 (1970).
- [35] D. B. Wetlaufer, S. K. Malik, L. Stoller, and R. L. Coffin. *J. Amer. Chem. Soc.*, **86**, 508 (1964).
- [36] B. Widom. *J. Chem. Phys.*, **39**, 2808 (1963).
- [37] T. L. Hill. *Statistical Mechanics, Principles and Selected Applications*, page 191. Dover Publications, New York (1987).

Chapter 1

Model of Freezing Behavior of Liquid Monolayers Adsorbed in Cylindrical Pores

1.1 Abstract

Freezing behavior of liquid monolayers adsorbed in extremely narrow tubes is studied by a lattice model that can be mapped to the Ising magnet. The model assumes an $m \times \infty$ square net with cylindrical geometry with m cells in the circular direction, each cell being occupied by a molecule with q orientations. First we examine how the freezing behavior of the model monolayer varies with increasing m , i.e., increasing the pore diameter. It is shown that the behavior in two dimensions ($m \rightarrow \infty$) is nearly achieved with small values of m ($m \sim 8$). Second we study an extended model that has anisotropic intermolecular interaction. When the anisotropic interaction energies are those with which the corresponding Ising model has antiferromagnetic interactions in the axial direction and ferromagnetic interactions in the circular direction, a semioordered phase appears in a temperature regime between those of solid and liquid states.

1.2 Introduction

Freezing of liquids confined in a cylindrical pore with nanoscale diameter has been extensively studied over the past few decades by experimental and theoretical methods [1, 2]. In experiments, phase behaviors of liquids adsorbed in nanopores and mesopores, such as those of carbon nanotubes

and MCM-41 materials, have been investigated using x-ray diffraction, neutron diffraction, NMR, and so on [3–9]. Commonly observed in such an extremely narrow cylinder is continuous freezing over some temperature range. Extensive studies have suggested that the sharpness of freezing strongly depends on confined substances, physical and chemical properties of porous materials, and the pore diameter [1]. As regards the effect of pore size, it is reported that water freezes gradually in pores of MCM-41 with average diameter of 1.2 nm while it freezes abruptly in pores with diameter of 1.75 nm [3]. Computer simulations have proved to be a powerful tool to explore a variety of one-dimensional solid phases in cylindrical pores [10–12] and theoretical studies provided a basic framework of understanding the effect of confinement [13, 14]. One of the main purposes of the present work is to examine the effect of pore diameter on the freezing behavior under extreme confinement.

A concrete example of liquids in less-than-two dimensions is a monolayer adsorbed on the inner surface of a cylindrical pore. When the pore diameter is of the order of molecular diameter the monolayer is essentially a one-dimensional liquid whereas it becomes a two-dimensional liquid as the pore diameter approaches a macroscopic size. We study here a lattice model relevant to such real systems. The model in one dimension has been studied earlier to illustrate the relation between the freezing behavior and the model parameters describing intermolecular interactions [15]. Now it is extended to the model in quasi-one dimension with a cylindrical geometry in order to examine the effect of pore diameter on the freezing behavior. As the temperature decreases, the model exhibits a gradual phase change from a high-energy, disordered state (liquid) to a low-energy, ordered state (solid). A notable feature of the model is that it can be mapped to the Ising model, which enables us to obtain the properties from those of the Ising magnet. We also examine an anisotropic model in which the interaction energy in the axial direction is different from that in the circular direction of the cylindrical geometry. This model exhibits an interesting two-step freezing behavior when the model parameters are chosen such that the corresponding anisotropic Ising model is antiferromagnetic in the axial direction and ferromagnetic in the circular direction.

1.3 Model

Figure 1.1 shows a monolayer of argon adsorbed in a cylindrical pore obtained by molecular

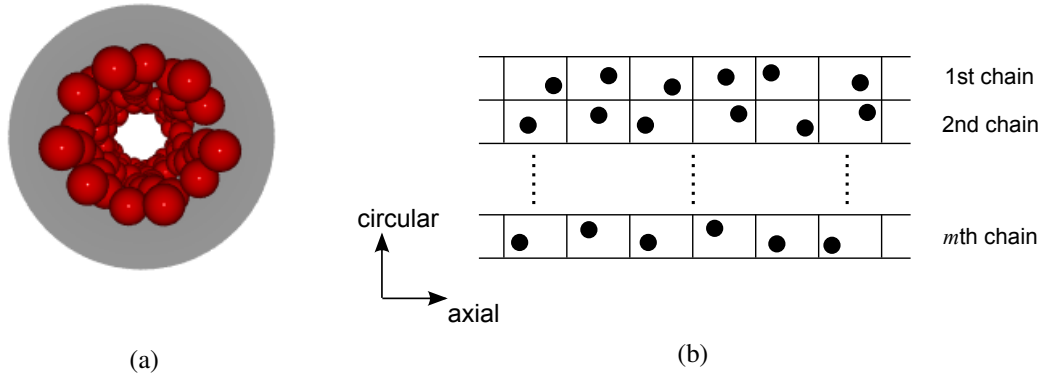


Figure 1.1: (a) A monolayer of argon adsorbed in a cylindrical pore and (b) $m \times \infty$ lattice of the model.

simulation (Fig. 1.1a) and the model liquid in quasi-one dimension (Fig. 1.1b). An inner surface of a cylindrical pore is divided into $m \times \infty$ lattice cells, each being occupied by one molecule. A molecule may be in any one of $q > 2$ states or orientations, one of which is a special one (state 1) and the other $q - 1$ are non-special ones (state 0, collectively). Two neighboring molecules interact with each other with the following interaction energies:

$$\begin{aligned}
 w & \quad \text{if both are in state 1 (bonded pair),} \\
 \epsilon \quad (> w) & \quad \text{if either one is in state 1 and the other is not (hetero pair),} \\
 u \quad (> w) & \quad \text{if neither is in state 1 (nonbonded pair).}
 \end{aligned} \tag{1.1}$$

The energy E of the system is given by the sum of the pair interaction energies. The system has the lowest energy and the lowest entropy when all the molecules are in the special orientation (state 1). The assumption $q > 2$, i.e., the number of non-special orientations being larger than 1, ensures that the more molecules in state 0, the larger the entropy of the system. (The orientation of each molecule may be continuous: Then $q - 1$ is a real number representing the ratio of a range of the non-special orientations to that of the special orientations.) It is then reasonable to assume that the system is in a solid state when the majority of molecules is in state 1 while it is in a liquid state when most of the molecules are in state 0.

The system with $m = 1$ is the one-dimensional lattice of coordination number $C = 2$ [15] and the system with $m = 2$ is the lattice of $C = 3$. When $m > 2$, we assume that the m -th chain in the lattice interacts with the first chain so that the square lattice forms an infinitely long cylinder ($C = 4$). Then, the number m of rows in Fig. 1.1b is a quantity proportional to the circumference of

the cylinder and so to the diameter. A main goal of the present study is to examine how the freezing behavior in one dimension approaches the one in two dimensions as m increases.

The energy of the system is written

$$E = wN_{11} + \epsilon N_{01} + uN_{00}, \quad (1.2)$$

where N_{11} , N_{01} and N_{00} are the numbers of bonded, hetero, and nonbonded pairs, respectively. Let N_1 and N_0 be the numbers of molecules in state 1 and state 0, and let $N = N_1 + N_0$, the number of molecules in the system. Then, from the identities

$$N_{11} + N_{01} + N_{00} = \frac{CN}{2} \quad \text{and} \quad CN_1 = 2N_{11} + N_{01} \quad (\text{or} \quad CN_0 = 2N_{00} + N_{01}),$$

the energy E is determined by specifying any one of N_1 and N_0 and any one of N_{11} , N_{01} , and N_{00} : here we choose N_1 and N_{01} and then

$$E = -\frac{C}{2}(u-w)N_1 + \frac{P}{2}(u-w)N_{01} + \frac{Cu}{2}N,$$

where

$$P = 1 + 2\frac{\epsilon - u}{u - w}. \quad (1.3)$$

Note that $P > -1$ because $u > w$ and $\epsilon > w$.

The partition function Z is the sum of $\exp(-E/kT)$ over all q^N configurations. But the energy E depends only on the arrangement of state 1 (the special orientation) and state 0 (any orientation other than the special one). Then, noting that the degeneracy for each site that is in state 0 is $q - 1$, the partition function Z is expressed as the sum over 2^N ways to assign state 0 and state 1 to the N lattice sites,

$$Z = \sum_{0,1} (q-1)^{N_0} \exp(-E/kT) = \sum_{0,1} \exp(-E'/kT), \quad (1.4)$$

where

$$E' = \left[-\frac{C}{2}(u-w) + kTQ \right] N_1 + \frac{P}{2}(u-w)N_{01} + \left[\frac{C}{2}u - kTQ \right] N \quad (1.5)$$

with

$$Q = \ln(q - 1). \quad (1.6)$$

Note $Q > 0$ because of $q > 2$.

The present model is equivalent to the spin- $\frac{1}{2}$ Ising model. The partition function (1.4) is identified with that of the Ising model on the underlying lattice with the magnetic field H and the spin-spin interaction energy parameter J at temperature T , provided that

$$H = \frac{C}{4}(u - w) - \frac{1}{2}kTQ, \quad (1.7)$$

$$J = \frac{P}{4}(u - w) \quad (1.8)$$

and spin \uparrow corresponds to state 1 and spin \downarrow to state 0. The corresponding Ising model is ferromagnetic, $J > 0$, if $P > 0$; it is antiferromagnetic, $J < 0$, if $P < 0$.

The fraction of the number of molecules in the special orientation (state 1)

$$\rho_1 = \left\langle \frac{N_1}{N} \right\rangle \quad (1.9)$$

will serve as an order parameter for the freezing behavior of the model: $\rho_1 = 1$ indicates a perfect solid state and $\rho_1 \sim 1/q = 1/(1 + e^Q)$ corresponds to a disordered liquid state. The temperature dependence of ρ_1 is obtained from the variation of M , the magnetization per spin in the Ising model, along the line of equation (1.7) in the T, H plane.

Let T_f be the temperature at which the magnetic field H of the corresponding Ising model is zero:

$$T_f = \frac{C(u - w)}{2kQ}.$$

Since H changes its sign at $T = T_f$ [Eq. (1.7)], it follows that $\rho_1 > \frac{1}{2}$ if $T < T_f$ and $\rho_1 < \frac{1}{2}$ if $T > T_f$. Now consider the systems with $P > 0$ (the corresponding Ising model being ferromagnetic). Then ρ_1 varies with T most rapidly around $T = T_f$ and so T_f may be regarded as a transition temperature. It is shown for the system in one dimension ($m = 1$) that ρ_1 reaches a minimum value at $T > T_f$ if and only if $P > 1$. That is, the ρ_1 minimum appears if the hetero pair is energetically less favorable than the nonbonded pair.

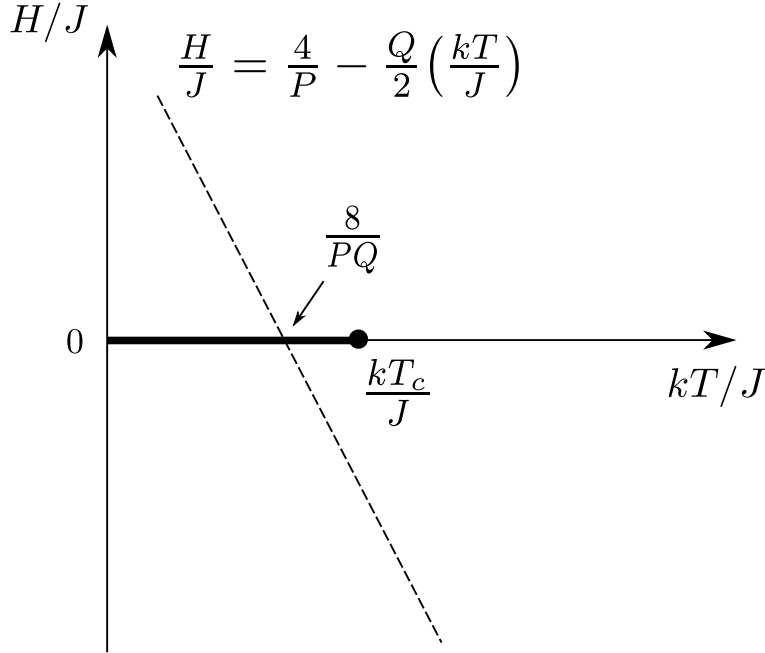


Figure 1.2: The locus of thermodynamic states of the model liquid on the T, H plane of the corresponding Ising model. The bold line is the phase boundary which terminates at the critical point $(H/J, kT/J) = (0, kT_c/J)$. The locus, shown as the dashed line, intersects the temperature axis at $8/PQ$.

The model liquid in less-than-two dimensions (m being finite) does not exhibit a first-order phase transition, as the corresponding Ising model does not [16]. (It exhibits the phase transition in the limit $P \rightarrow \infty$ or $Q \rightarrow \infty$ even if m is finite [15].) In the limit $m \rightarrow \infty$, as we shall see, our model shows both a gradual phase change and a first-order transition, depending on the model parameters. Figure 1.2 shows the phase diagram for the 2-d Ising ferromagnet on the T, H plane. The line of singularity lies on the temperature axis from 0 to the critical point kT_c/J . In the same diagram, as shown by the dashed line, the temperature variation of the present model follows the line

$$\frac{H}{J} = \frac{4}{P} - \frac{Q}{2} \left(\frac{kT}{J} \right), \quad (1.10)$$

which follows from (1.7) and (1.8). Therefore, the model liquid exhibits a first-order transition if the point where the dashed line, Eq. (1.10), intersects the temperature axis is below the critical

point, i.e., if $kT_f/J < kT_c/J = 2.26185\dots$ [17], or, since $kT_f/J = 8/PQ$,

$$PQ > 3.525494\dots \quad (1.11)$$

Otherwise, freezing in our model liquid remains continuous even in the limit of $m \rightarrow \infty$.

1.4 Isotropic model: Effect of pore diameter on freezing

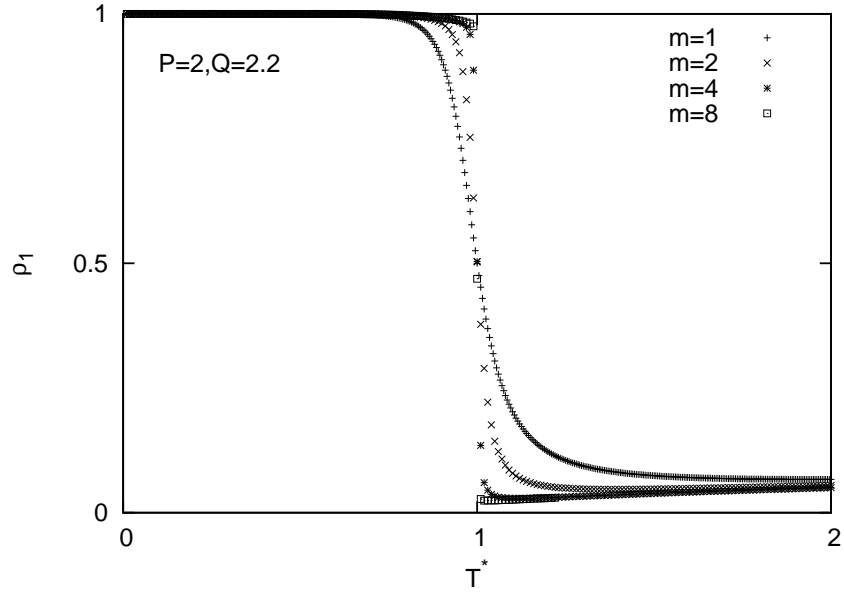
Properties of the model liquid are obtained from those of the corresponding Ising model via the mapping relations (1.7) and (1.8). Thus we performed Monte Carlo simulations of the spin- $\frac{1}{2}$ Ising model of the $m \times n$ square net, where m is the number of lattice sites in the circular direction in Fig. 1.1b, varying from 1 to 8. As remarked earlier, m is a measure of the diameter of the cylindrical pore in which a liquid monolayer is adsorbed. On the other hand, n is the number of lattice sites of each row parallel to the cylinder axis. In the simulation, n is taken to be 1000, which is sufficiently large that the phase behavior is essentially the same as that of an infinitely-long system. The periodic boundary condition is imposed on the axial direction, too. For each state point, the average quantities are obtained from a production run of 10^8 MC steps, each step being a set of trial moves of $m \times n$ spins.

For various sets of parameters P and Q , the variation of ρ_1 is obtained as a function of the dimensionless temperature:

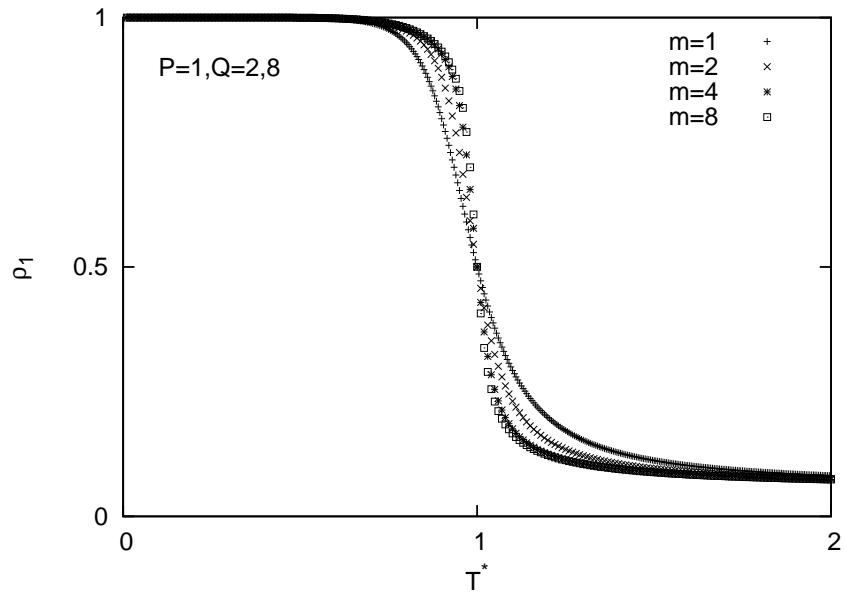
$$T^* = \frac{T}{T_f} = \frac{2kTQ}{C(u-w)}. \quad (1.12)$$

Note that $T^* = 1$ means $H = 0$ in the corresponding Ising model. Figure 1.3 shows the variation of ρ_1 for the model liquid with (a) $P = 2$, $Q = 2.2$ and (b) $P = 1$, $Q = 2.8$. Here the values are chosen so that the former satisfies (1.11) and the latter does not, that is, the former system in two dimensions ($m \rightarrow \infty$) exhibits a first-order phase transition whereas the latter system does not. The results for $m = 1$ are those obtained from the explicit formula for ρ_1 in the one-dimensional study [15].

In both cases, the rate of variation of ρ_1 with T^* around $T^* = 1$ becomes larger as m increases, that is, the freezing behavior becomes sharper. When $m = 8$ in case (a), the phase behavior is indistinguishable from the first-order phase transition. In case (b), the result of $m = 4$ and that of



(a) $P = 2, Q = 2.2 \left(\frac{8}{PQ} < \frac{kT_c}{J} \right)$



(b) $P = 1, Q = 2.8 \left(\frac{8}{PQ} > \frac{kT_c}{J} \right)$

Figure 1.3: The temperature dependence of ρ_1 of the model liquid: (a) $P = 2, Q = 2.2$ and (b) $P = 1, Q = 2.8$.

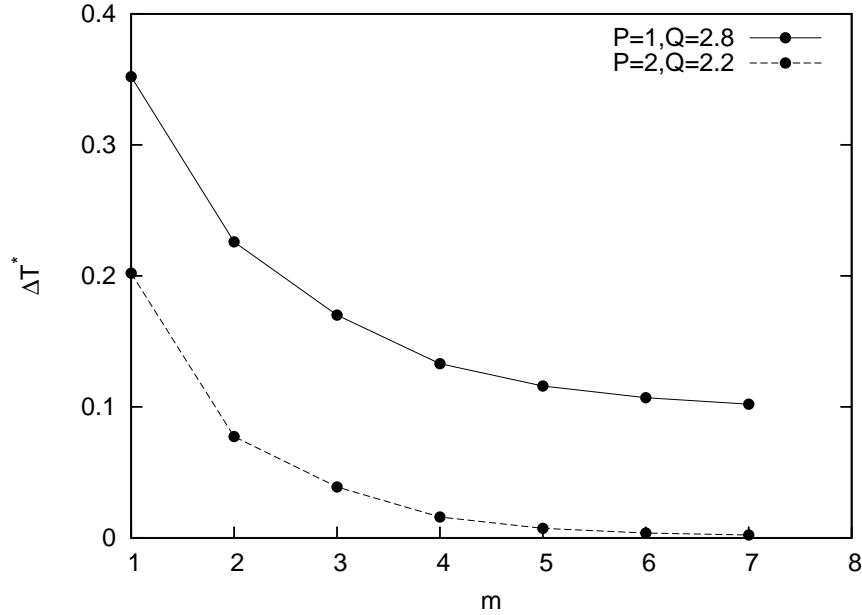


Figure 1.4: The sharpness of freezing ΔT^* as a function of the number m of rows, which is proportional to the pore diameter.

$m = 8$ are almost identical, showing that the phase behavior is very close to the limiting behavior in two dimensions (in this case a continuous phase behavior) when $m \geq 4$. These results, therefore, show that the limiting behavior in two dimensions is nearly achieved for small values of m . This will be seen clearly if the sharpness of freezing is measured by the quantity

$$\Delta T^* = - \left. \frac{dT^*}{d\rho_1} \right|_{T^*=1}. \quad (1.13)$$

ΔT^* can be considered as the temperature range over which much of the phase change occurs. As shown in Fig. 1.4, ΔT^* greatly decreases as m increases from 1 to 4, both in case (a) and in case (b).

In case (a), as displayed in Fig. 1.3a, there exists a minimum of $\rho_1(T^*)$ at $T^* > 1$. (That is not apparent for $m = 1$ but analytical calculation shows that the minimum is at $T^* = 1.997 \dots$) The result is consistent with the condition that $\rho_1(T^*)$ in one dimension exhibits a minimum. The implication and the condition of the appearance of the nonmonotonic behavior in the temperature range of a liquid state are subjects beyond the present work.

1.5 Anisotropic model: Effect of anisotropy on freezing

An interesting extension of the model of a liquid adsorbed in a cylindrical pore is to introduce anisotropy in the intermolecular interaction, i.e., to assume different values of the interaction energies w , ϵ , and u in Eq. (1.1) for neighboring molecules aligned parallel to and those aligned perpendicular to the cylinder axis. The introduction of anisotropy is obviously a generalization of the original isotropic model, lifting the restriction of the interaction parameters. A main purpose of the extension here is, however, not to scrutinize general features of the model but to examine freezing behaviors qualitatively different from those previously studied.

We consider again a square lattice of cylindrical geometry but now assume the parameter set (w , ϵ' , and u) for the circular direction different from the set (w , ϵ , and u) for the axial direction. Note that the interaction energy for the hetero pair alone is taken to be anisotropic. In the following discussion, $m > 2$ is assumed, and so the coordination number C is 4. As in the isotropic case, the partition function can be written

$$Z = \sum_{0,1} \exp(-E'/kT), \quad (1.14)$$

but now with

$$E' = \left[-2(u - w) + kTQ \right] N_1 + \frac{P}{2}(u - w)N_{01}^A + \frac{P'}{2}(u - w)N_{01}^C + \left[2u - kTQ \right] N, \quad (1.15)$$

where N_{01}^A and N_{01}^C are the numbers of hetero pairs in the axial and circular directions, respectively, and

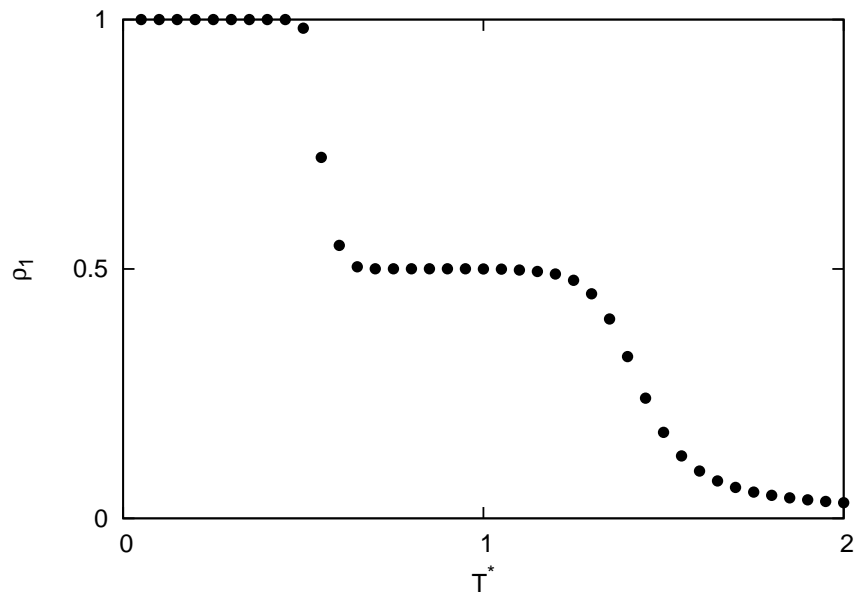
$$P = 1 + 2\frac{\epsilon - u}{u - w}, \quad P' = 1 + 2\frac{\epsilon' - u}{u - w}. \quad (1.16)$$

The corresponding Ising model is also anisotropic and is related to the model liquid by

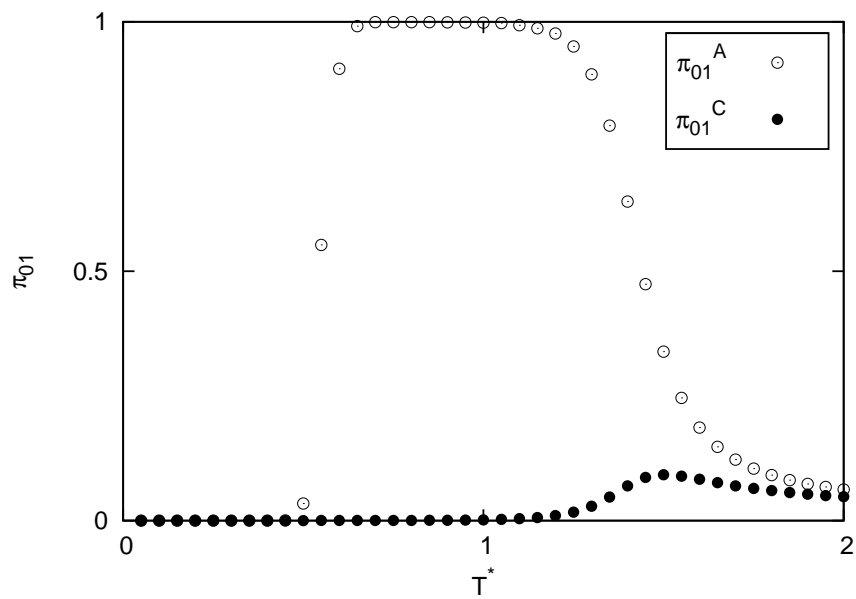
$$H = (u - w) - \frac{kTQ}{2}, \quad J = \frac{P}{4}(u - w), \quad J' = \frac{P'}{4}(u - w), \quad (1.17)$$

where J and J' are the spin-spin interaction in the axial and circular directions. An interesting phase behavior is found when $P < 0$ and $P' > 0$, i.e., when the corresponding anisotropic Ising model is antiferromagnetic along the axial direction and ferromagnetic along the circular direction.

Figure 1.5 shows the simulation results for $m = 8$, $P = -0.9$, $P' = 2$ and $Q = 5$. The dimensionless



(a)



(b)

Figure 1.5: The temperature dependence of ρ_1 (a) and π_{01}^A , π_{01}^C (b) of the anisotropic model liquid with $m = 8$, $P = -0.9$, $P' = 2$, and $Q = 5$.

temperature T^* is the same as in (1.12). The temperature dependence of ρ_1 , the ratio of molecules in state 1 is shown in Fig. 1.5a, and the temperature dependences of

$$\pi_{01}^A = \left\langle \frac{N_{01}^A}{N} \right\rangle, \quad \pi_{01}^C = \left\langle \frac{N_{01}^C}{N} \right\rangle$$

are given in Fig. 1.5b. In the ρ_1 - T^* plot, there is a temperature range around $T^* = 1$ where ρ_1 is nearly constant ($\rho_1 \sim 0.5$). In that range, $\pi_{01}^A \sim 1$ whereas $\pi_{01}^C \sim 0$. This means almost all the neighboring molecules in the axial direction are hetero pairs, while it is almost the case that any ring of m molecules in the circular direction does not contain a hetero pair. In other words, a frozen, solid-like ring and a disordered, liquid-like ring alternate with each other along the cylindrical axis. Thus, in this temperature regime, the system is in a semiordered state. This type of two-step freezing (from liquid to semiorder to solid) can be found only if $P < 0$ and $P' > 0$ ($u - \epsilon > \epsilon - w$, $u - \epsilon' < \epsilon' - w$); a different type of two-step freezing is observed if both P and P' are negative. In the limit $Q \rightarrow \infty$, the two-step freezing is represented by a step function of T^* . This is because all the temperatures T corresponding to finite T^* go to 0 as $Q \rightarrow \infty$ [see (1.12)] and so the system with infinitely large Q is in the lowest energy state at any finite T^* . Then all the neighboring molecules in the circular direction must be bonded or nonbonded, i.e., $N_{01}^C = 0$, when $P' > 0$. The solid-semiorder and semiorder-liquid transitions occur at $T_1^* = 1 - \frac{|P|}{2}$ and $T_2^* = 1 + \frac{|P|}{2}$, respectively, and the temperature range $T_2^* - T_1^*$ of the semiordered phase is $|P|$. Note that the result is independent of P' (as long as P' is positive), for the Hamiltonian (1.15) does not depend on P' when $N_{01}^C = 0$.

References

- [1] H. K. Christenson. *J. Phys. Condens. Matter*, **13**, R95 (2001).
- [2] C. Alba-Simionesco, B. Coasne, G. Dosseh, G. Dudziak, K. Gubbins, R. Radhakrishnan, , and M. Sliwiska-Bartkowiak. *J. Phys. Condens. Matter*, **18**, R15 (2006).
- [3] K. Morishige and K. Kawano. *J. Chem. Phys.*, **110**, 4867 (1999).
- [4] Y. Maniwa, H. Kataura, M. Abe, S. Suzuki, Y. Achiba, H. Kira, , and K. Matsuda. *J. Phys. Soc. Jpn.*, **71**, 2863 (2002).

- [5] E. Liu, J. Dore, J. Webber, D. Khushalani, S. Jähnert, G. Findenegg, and T. Hansen. *J. Phys. Condens. Matter*, **18**, 10009 (2006).
- [6] S. Jähnert, F. Chávez, G. Schaumann, A. Schreiber, M. Schönhoff, and G. Findenegg. *Phys. Chem. Chem. Phys.*, **10**, 6039 (2008).
- [7] G. Buntkowsky, H. Breitzke, A. Adamczyk, F. Roelofs, T. Emmeler, E. Gedat, B. Grünberg, Y. Xu, H. Limbach, J. Shenderovich, A. Vyalikh, and G. Findenegg. *Phys. Chem. Chem. Phys.*, **9**, 4843 (2007).
- [8] G. Findenegg, S. Jähnert, D. Akcakayiran, and A. Schreiber. *ChemPhysChem*, **9**, 2651 (2008).
- [9] S. Kittaka, S. Ishimaru, M. Kuranishi, T. Matsuda, and T. Yamaguchi. *Phys. Chem. Chem. Phys.*, **8**, 3223 (2006).
- [10] G. Pickett, M. Gross, , and H. Okuyama. *Phys. Rev. Lett.*, **85**, 3652 (2000).
- [11] K. Koga, G. Gao, H. Tanaka, , and X. Zeng. *Nature*, **412**, 802 (2001).
- [12] K. Koga and H. Tanaka. *J. Chem. Phys.*, **124**, 131103 (2006).
- [13] R. Evans. *J. Phys. Condens. Matter*, **2**, 8989 (1990).
- [14] D. Wilms, A. Winkler, P. Virnau, , and K. Binder. *Phys. Rev. Lett.*, **105**, 045701 (2010).
- [15] K. Koga. *J. Chem. Phys.*, **118**, 7973 (2003).
- [16] E. Montroll. *J. Chem. Phys.*, **9**, 706 (1941).
- [17] L. Onsager. *Phys. Rev.*, **65**, 117 (1944).

Chapter 2

Local solubility of nonpolar molecules in the liquid-vapor interfaces of water and simple liquids

2.1 Abstract

The local solubility Σ of nonpolar molecules at the liquid-vapor interface of water and that at the interface of simple liquids are examined for model systems. For Lennard-Jones (LJ) solutes in model water and those in the LJ solvent, Σ is obtained by the Widom test particle method as a function of the coordinate normal to the interface. In order to examine the effect of the solvent structure on Σ , we compare the dependence of Σ on a reduced coarse-grained density of the solvent ρ_{cg}^* for water with that for the LJ solvent under the condition that ε/T is common for the two systems, where ε is the LJ energy parameter between solute and solvent molecules and T is the temperature. We found that the solubility Σ of the LJ solute is higher in water than in the LJ solvent at any given ρ_{cg}^* , i.e., structure of water has higher ability to dissolve the nonpolar molecule than that of simple liquids, not only in their liquid states but also in their interfacial regions. This is partly because the probability of forming a sufficiently large cavity is higher in water than in the LJ fluid, as confirmed by the calculation of the local solubility of the hard-sphere solute. In addition, it is found that variation of the probability of cavity formation with ρ_{cg} in water is very similar to that in the LJ solvent if ρ_{cg} is scaled with the bulk liquid density.

2.2 Introduction

Much attention has been paid to the behavior of solute molecules at the liquid-vapor interface, where the density of solvent varies rapidly within a distance of few molecular diameters [1–8]. Surface-specific spectroscopic techniques, such as second-harmonic generation (SHG) and sum-frequency generation (SFG) [2, 3, 9], are used to investigate solute molecules adsorbed at interfaces. Application of these methods ranges from investigating the orientation and the hydration structure of small molecules at the air-water interface [10–13] to detecting the structure and phase transitions in a dense monolayer of surfactant at the interface [1, 14–16]. However, the spacial distribution of solute species in the interface has not been determined from experiments.

Molecular-scale information on the solvation in the liquid-vapor interface can be obtained by computer simulation [4–8, 17]. A fundamental question is how the solubility of a solute varies with the height z through an interface. The spacial dependence of the solubility can be described by the excess chemical potential μ_{ex} of the solute as a function of z . There are many studies on the calculation of $\mu_{\text{ex}}(z)$ of various molecules in the liquid-vapor interface of water [18–23]. The common behavior of $\mu_{\text{ex}}(z)$ obtained for hydrophobic solutes is as follows: (i) it has a minimum at the interface, i.e., solutes are surface active; (ii) its value at the bulk liquid phase is very high, i.e., the solubility in the bulk water is very small; and (iii) there is a free energy barrier around the liquid-side of the interface.

The solvation in the liquid-vapor interface of simple fluids is not well studied [24] as compared to that of water. For example, the profiles of $\mu_{\text{ex}}(z)$ are still unknown for nonpolar, monatomic gases at the interface. One of the purposes of the present study is to examine whether or not the behavior of $\mu_{\text{ex}}(z)$ of hydrophobic solutes in the interface of water is qualitatively different from that in the interface of simple liquids.

An intuitive understanding of the solvation at infinite dilution is gained by the Widom test-particle theory [25–27]. At infinite dilution, the excess chemical potential of a solute at position \mathbf{r} in a solvent is expressed as an average of the Boltzmann factor $e^{-\Psi/kT}$ over the canonical ensemble of the solvent

$$\mu_{\text{ex}}(\mathbf{r}) = -kT \ln \left\langle e^{-\Psi(\mathbf{r})/kT} \right\rangle, \quad (2.1)$$

where T is the temperature and k is Boltzmann’s constant. $\Psi(r)$ is the interaction energy of the

test particle (solute molecule) fixed at r with all solvent molecules. When the test particle overlaps with any one of solvent molecules, the solute-solvent interaction energy is infinitely high, and then the Boltzmann factor is essentially zero. For the Boltzmann factor to be nonzero, a cavity larger than the size of the solute molecule has to be formed at r . If the cavity is sufficiently large, the Boltzmann factor is greater than 1, for then the solute-solvent attractive interactions make Ψ less than 0. The strength of attraction increases with the number of solvent molecules in the vicinity of the cavity. Thus, there are two aspects of the structure of solvent which are relevant to the solubility of nonpolar solutes. One is the probability of cavity formation and the other is the coordination number of the solvent molecules around the cavity.

Another factor that affects the solubility is a pair interaction energy between solute and solvent molecules divided by kT . Let us compare methane in water with methane in krypton, both near the triple point. With the Lennard-Jones (LJ) energy parameters ε_{AB} chosen for the two systems [28, 29], one finds that $\varepsilon_{AB}/kT \sim 0.4$ for methane in water and ~ 1.3 for methane in krypton. In part, this difference explains the low solubility of methane in water as compared to that of methane in krypton. Therefore, both the effect of solvent structure and that of the characteristic pair interaction energy divided by kT should be considered, when local solubilities of various systems are compared.

We compare the solubility profiles of small, nonpolar molecules in the liquid-vapor interface of water with that in the interface of the LJ liquid. For both systems, the solute-solvent interaction is described by the LJ potential, that is, the solute is the LJ particles. The density profile of solvent molecules is obtained by molecular dynamics simulation and $\mu_{\text{ex}}(z)$ is calculated by the Widom test particle method as in previous studies [20, 30–32].

In order to clarify the effect of the solvent structure on the local solubility, we present the results and analyses in the following order. First, we compare behavior of $\mu_{\text{ex}}(z)$ in water with that in the LJ solvent under the condition that the reduced solute-solvent LJ parameters σ^* and ε^* are common for the two systems *and* the temperature is close to the triple point of each solvent. The σ^* and ε^* are the solute-solvent LJ parameters σ_{AB} and ε_{AB} divided by the solvent-solvent LJ parameters σ_{BB} and ε_{BB} , respectively. Second, we express μ_{ex} as functions of a solvent density which varies through the interface and compare μ_{ex} for water with that for the LJ fluid. This enables us to examine the difference in μ_{ex} between the two systems eliminating the contribution from the density difference.

Third, we make the same comparison under the condition that ε_{AB}/kT is common for the two systems. Then we may examine the difference in μ_{ex} that arises only from the difference in solvent structure. Finally, we also compare the probability of cavity formation in the interface of water with that in the interface of the LJ solvent. The present calculation suggests that the probability of cavity formation in the liquid-vapor interface is a universal function of a solvent density scaled by that of the coexisting liquid phase.

2.3 Theory

Suppose that the system is composed of N_A solute and N_B solvent molecules in a fixed volume V , that it is in a state of the liquid-vapor coexistence, and that the solute and solvent local densities ρ_A and ρ_B vary only in one direction. Let the z -axis be in that direction, which is normal to the liquid-vapor interface, with $z < 0$ in the gas phase, $z > 0$ in the liquid phase, and $z = 0$ at the Gibbs equimolar dividing surface [33] for the solvent density. This mathematical surface divides V into V^g and V^l , volumes of the gas and liquid regions, in the way the following condition is satisfied:

$$\rho_B^g V^g + \rho_B^l V^l = N_B, \quad (2.2)$$

where ρ_B^g and ρ_B^l are the solvent densities of the homogeneous gas and liquid phases at the two-phase equilibrium.

In what follows, we consider infinitely-dilute solutions: $N_A/V \rightarrow 0$. Let us define the local solubility $\Sigma(z)$ at the position z by

$$\Sigma(z) = \frac{\rho_A(z)}{\zeta_A}, \quad (2.3)$$

where ζ_A is the activity of the solute defined such that $\zeta_A \rightarrow \rho_A$ as $\rho_A \rightarrow 0$ and $\rho_B \rightarrow 0$. Then, $\Sigma(z) \simeq 1$ in the homogeneous gas phase ($z \rightarrow -\infty$) and $\Sigma(z) \simeq \rho_A^l/\rho_A^g$ in the homogeneous liquid phase ($z \rightarrow +\infty$), the latter of which is the equilibrium ratio of the solute density in the liquid phase to that in the gas phase (the Ostwald absorption coefficient). The local excess chemical potential $\mu_{\text{ex}}(z)$ is related to $\Sigma(z)$ via $\mu_{\text{ex}}(z) = -kT \ln \Sigma(z)$.

The activity ζ_A of the solute at infinite dilution is by definition

$$\zeta_A = \frac{Q_0}{Q_1}, \quad (2.4)$$

where Q_0 and Q_1 are the configuration integrals of the system with $N_A = 0$ (system 0) and the system with $N_A = 1$ (system 1), respectively. Note that ζ_A is uniform throughout the system as are the chemical potential μ_A and the temperature T . Let $\Psi(\mathbf{r}) = \Psi(\mathbf{r}, \mathbf{r}_1, \dots, \mathbf{r}_{N_B})$ be the interaction energy of the solute molecule at \mathbf{r} with N_B solvent molecules at $\mathbf{r}_1, \dots, \mathbf{r}_{N_B}$ and $U_0 = U_0(\mathbf{r}_1, \dots, \mathbf{r}_{N_B})$ and $U_1(\mathbf{r}) = U_1(\mathbf{r}, \mathbf{r}_1, \dots, \mathbf{r}_{N_B})$ be the potential energies of system 0 and that of system 1, respectively. Noting that $U_1(\mathbf{r}) = \Psi(\mathbf{r}) + U_0$, Eq. (2.4) is now written

$$\zeta_A = \frac{\frac{1}{Q_1} \int \exp(-U_1(\mathbf{r})/kT) d\mathbf{r}^{N_B}}{\frac{1}{Q_0} \int \exp(-\Psi(\mathbf{r})/kT) \exp(-U_0/kT) d\mathbf{r}^{N_B}} = \frac{\rho_A(\mathbf{r})}{\langle \exp(-\Psi(\mathbf{r})/kT) \rangle}, \quad (2.5)$$

where $\langle \dots \rangle$ means the average with the factor $\exp(-U_0/kT)/Q_0$ over the coordinates of solvent molecules (i.e., the average over the configuration in system 0) and $\rho_A(\mathbf{r})$ is the local density of solute at position \mathbf{r} in system 1. Since the system is homogeneous in any plane normal to the z axis, the numerator and denominator are functions of z alone. The local solubility defined in Eq. (2.3) is then

$$\Sigma(z) = \langle \exp(-\Psi(z)/kT) \rangle. \quad (2.6)$$

This is the potential distribution theorem for inhomogeneous systems [27] and what we will use for calculating the local solubility $\Sigma(z)$ of solutes through the liquid-vapor interface of the model systems described below.

2.4 Methods

We consider two model solvents: the TIP4P/2005 model water [29] and the LJ solvent. Each molecule of the model water has one LJ interaction site on the oxygen atom with the size and energy parameters $\sigma_{BB} = 3.1589 \text{ \AA}$ and $\varepsilon_{BB}/k = 93.2 \text{ K}$ and three Coulomb interaction sites. In both solvents, the pair interaction between solvent and nonpolar-solute molecules is taken to be the LJ potential function and the LJ parameters, σ_{AB} and ε_{AB} , are varied in order to examine the effects

of the solute size and the strength of solute-solvent attraction on the local solubility.

To obtain equilibrium configurations of the liquid-vapor interface, we carried out the *NVT*-ensemble molecular dynamics simulation of the model water and the LJ solvent. The program package GROMACS 4.5.5 [34] was employed for the model system of pure water and our own MD program was used for the LJ solvent. The simulation cell is a rectangular box ($L_x = L_y < L_z$) and contains 1372 solvent molecules under the periodic boundary conditions in the three directions. The temperature is fixed at $T = 273$ K for water and $T^* = kT/\sigma_{\text{BB}} = 0.7$ for the LJ solvent using the Nosé [35] or Nosé-Hoover [36, 37] thermostat. The initial configuration is prepared by placing a dense-liquid slab of molecules in the middle of the rectangular cell. The configuration is sampled every 100 steps after the equilibration period of 1×10^6 steps. There are two liquid-vapor interfaces in each equilibrium configuration.

In the simulation of pure water, we set $L_x = L_y = 37.15$ Å and $L_z = 111.5$ Å. Both the Coulomb and LJ parts of the intermolecular interaction are smoothly truncated between 12 and 13 Å using a switching function. The Coulomb interaction is treated by the particle mesh Ewald method. The time step is 1 fs. For the LJ solvent, the simulation box has the dimensions $L_x = L_y = 11.76 \sigma_{\text{BB}}$ and $L_z = 35.29 \sigma_{\text{BB}}$. The LJ interaction is gradually switched off between $3.91 \sigma_{\text{BB}}$ and $4.50 \sigma_{\text{BB}}$. The dimensionless time-step $\Delta t^* = \Delta t \sqrt{\epsilon_{\text{BB}}}/(\sigma_{\text{BB}} \sqrt{m})$ is chosen to be 4.6×10^{-4} , where m is the mass of the particle.

The equilibrium configurations of the solvents obtained by simulation are used for the particle insertion calculation. Before performing the particle insertion, we calculate the Gibbs equipolar dividing surface every 2×10^5 steps to redefine the origin of the z -axis. This procedure is essential to ensure that the relative distance between the test particle and the dividing surface is invariant for each insertion; otherwise, $\Sigma(z)$ would be undesirably broadened due to the translational motion of the interface in the course of simulation. The test particle (solute molecule) is inserted into 70×70 lattice points on the plane of constant z defined with respect to each interface: note there are two interfaces in the system. The total number of the trial insertions at each z in the set of equilibrium configurations is about 5×10^9 . The local solubility $\Sigma(z)$ is then obtained by varying z with an interval of $0.10 \sigma_{\text{BB}}$.

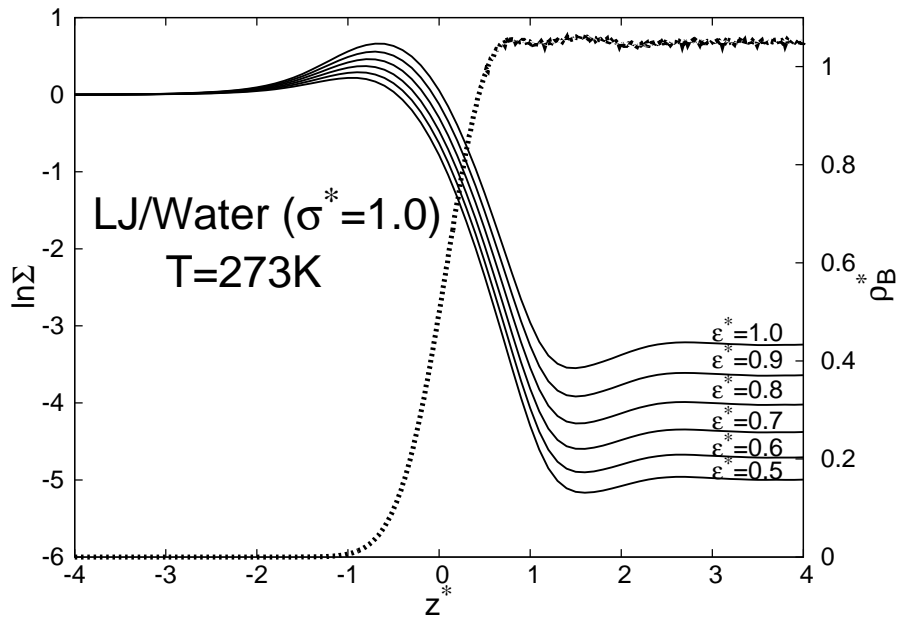
2.5 Results

Behavior of $\Sigma(z)$ near the triple point

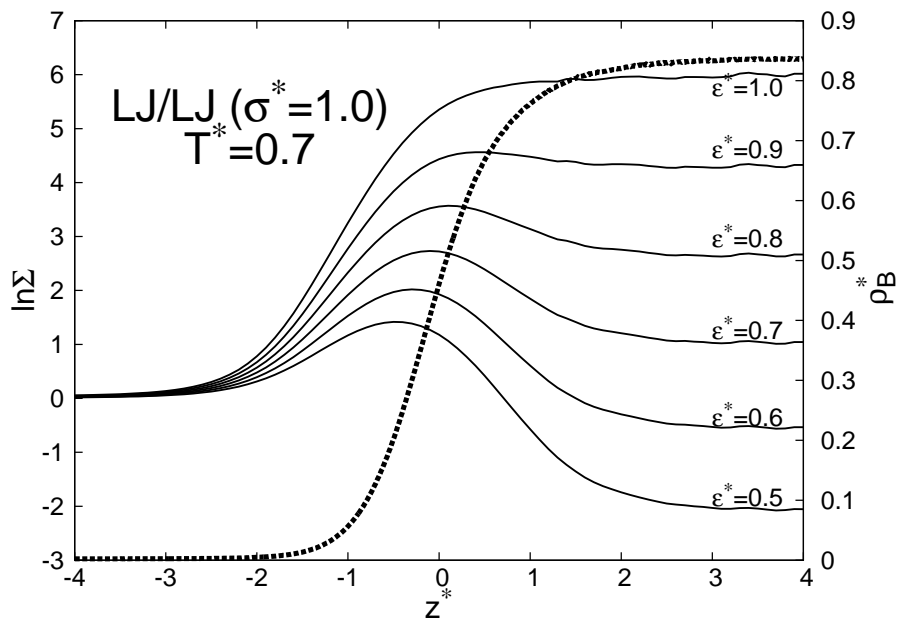
In Fig. 2.1, we show the local solubility (in the logarithmic scale) of LJ solutes (a) in water at $T = 273$ K and (b) in the LJ solvent at $T^* = 0.7$, together with the reduced local density $\rho_B^*(z^*) = \sigma_{BB}^3 \rho_B(z^*)$ of the solvent, as functions of $z^* = z/\sigma_{BB}$. The thermodynamic state of the model systems is specified by temperature alone because the infinitely-dilute solutions (solvents) are one-component, two-phase systems. In both cases, the liquid, gas, and the interface examined here are in a state close to the triple point. The profiles $\ln \Sigma(z^*)$ in Fig. 2.1 are those obtained for six different solutes with the solute-solvent LJ parameters $\varepsilon^* = \varepsilon_{AB}/\varepsilon_{BB} = 0.5, 0.6, \dots, 1$ and $\sigma^* = \sigma_{AB}/\sigma_{BB} = 1$.

Both in water and in the LJ solvent, $\ln \Sigma(z^*) \simeq 0$, or equivalently $\Sigma \simeq 1$, for the gas-phase region ($z^* < -3$). This is what we have anticipated earlier. In case of water (Fig. 2.1a), $\ln \Sigma$ exhibits a local maximum on the vapor side of the interface (in a range $-1 < z^* < 0$) and a local minimum on the liquid side (in a range $1 < z^* < 2$) and varies rapidly in a narrow range including the equimolar surface $z^* = 0$. That $\ln \Sigma(z^*) < 0$ deep inside the liquid region indicates $\mu_{\text{ex}}(z^*) > 0$. The local maximum in $\ln \Sigma$ is equivalent to a local minimum in $\mu_{\text{ex}}(z^*)$: it is the manifestation of the interface adsorption of the solute. The local minimum in $\ln \Sigma$ means a local maximum in $\mu_{\text{ex}}(z^*)$, which has been observed as the free energy barrier in earlier works [6, 18, 21]. It is clear in Fig. 2.1a that $\ln \Sigma(z^*)$ at any fixed z^* increases with increasing the solute-solvent LJ energy parameter ε^* .

In the LJ solvent, too, $\ln \Sigma(z^*)$ at any given z^* increases as ε^* increases. When $\varepsilon^* = 1.0$, i.e., the solute molecule is identical to the solvent molecule, there is no maximum in $\Sigma(z^*)$ whereas for all $\varepsilon^* \leq 0.9$, the adsorption at interface is observed. With $\varepsilon^* \geq 0.7$, $\Sigma(z^*)$ in the liquid-phase region ($z^* \simeq 4$) is greater than 1, i.e., the solute molecule favors the liquid phase than the gas phase. This is in contrast to the case of water for which we found $\Sigma(z^* \simeq 4) < 1$ for all ε^* examined. The LJ solute in the LJ solvent exhibits both the interface adsorption and the negative $\ln \Sigma(z^*)$ in the liquid-phase region if $\varepsilon^* \leq 0.6$, that is, only if the solute-solvent attractive interaction is much weaker than the solvent-solvent one. On the other hand, LJ solutes in water exhibit both of the features even if ε^* is as large as 1.5. However, this condition for water does not mean that the solute-solvent attractive interaction is stronger than the solvent-solvent one because in case of water a large part of the intermolecular attraction arises from the Coulomb interactions.



(a)



(b)

Figure 2.1: The local solubility of LJ solutes in the logarithmic scale $\ln \Sigma(z^*)$ (solid lines) and the reduced density profile $\rho_B^*(z^*)$ of the solvent (dashed line) for (a) water at $T = 273$ K and (b) the LJ solvent at $T^* = 0.7$. The reduced coordinate $z^* = z/\sigma_{BB}$ and $\rho_B^*(z^*) = \sigma_{BB}^3 \rho_B(z^*)$. The $z^* = 0$ is the Gibbs equimolar surface.

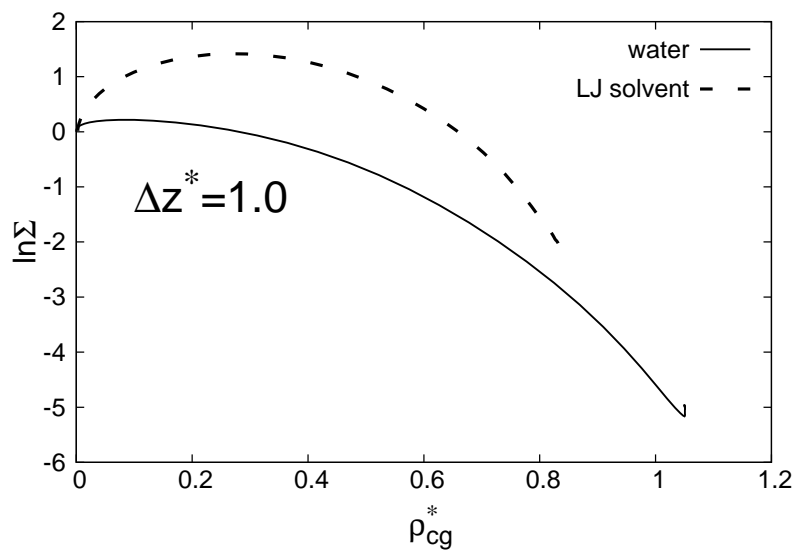
Effect of the solvent structure on the solubility

The local solubility $\Sigma(z)$ at given z for water and that for the LJ solvent differ significantly even though both solvents are in states close to their triple points and both systems have the same solute-solvent pair potential function. A possible reason for the difference in $\Sigma(z)$ is difference in the reduced solvent density $\rho_B^*(z)$ at given z . To exclude this effect, we plot $\ln \Sigma$ against ρ_{cg}^* in Fig. 2.2, where ρ_{cg}^* is $\rho_B^*(z^*)$ averaged over a range $[z^* - \Delta z^*, z^* + \Delta z^*]$ and is referred to as the coarse-grained solvent density. Note that both $\ln \Sigma$ and ρ_{cg}^* are functions of z^* but now we examine how $\ln \Sigma$ changes with ρ_{cg}^* as z varies through the interface. Two choices of Δz^* are employed for ρ_{cg}^* : $\Delta z^* = 1$ (Fig. 2.2a) and $\Delta z^* = 2$ (Fig. 2.2b). In either case, the local solubility in the LJ solvent is higher than that in water at any given ρ_{cg}^* when the solute-solvent LJ parameters σ^* and ε^* are common and the temperature is close to the triple point.

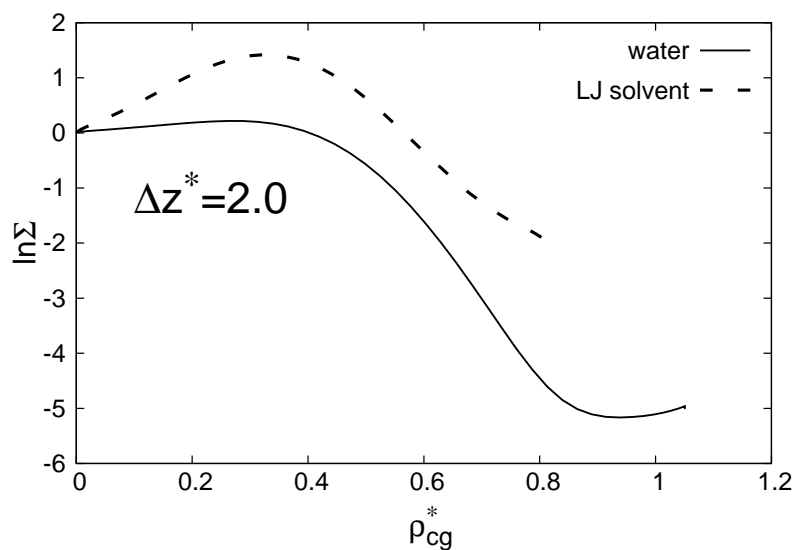
Now we compare the plots of $\ln \Sigma$ vs ρ_{cg}^* for the two solvents when σ^* and $\varepsilon^*/T^* = \varepsilon_{AB}/kT$ are common. The reason we choose ε^*/T^* to be common is that then one may examine the effect of the solvent structure on Σ , excluding the effect of temperature. Under this condition we would find the same Σ if the solvent structures were the same for the two different systems with different temperatures, because the solubility Σ of the LJ solute is a function of σ^* and ε^*/T^* . We have chosen $\varepsilon^* = 2.09$ for water and $\varepsilon^* = 0.50$ for the LJ solvent so that $\varepsilon^*/T^* = 5/7$, a common value for the two systems. Figure 2.3 shows that in either choice of Δz^* , the solubility in water is higher than that in the LJ solvent. This is opposite to what we have found in Fig. 2.2. Nonpolar solutes (LJ particles) are more soluble in water than in the LJ solvent for any given solvent density ρ_{cg}^* in the liquid-vapor interfacial region if the solute-solvent σ^* and ε^*/T^* are chosen to be common. Also, the solubility in bulk liquid water is higher than that in the bulk LJ liquid if σ^* and ε^*/T^* are common for the two systems. The latter is observed for other values of ε^*/T^* ($= 6/7, 7/7, \dots, 15/7$), too.

Difference in the probability of cavity formation between water and the Lennard-Jones solvent

In the previous subsection, we have seen that the model water with its liquid-vapor interface has higher ability to dissolve the LJ solute at given solvent density ρ_{cg}^* than that of the LJ solvent with

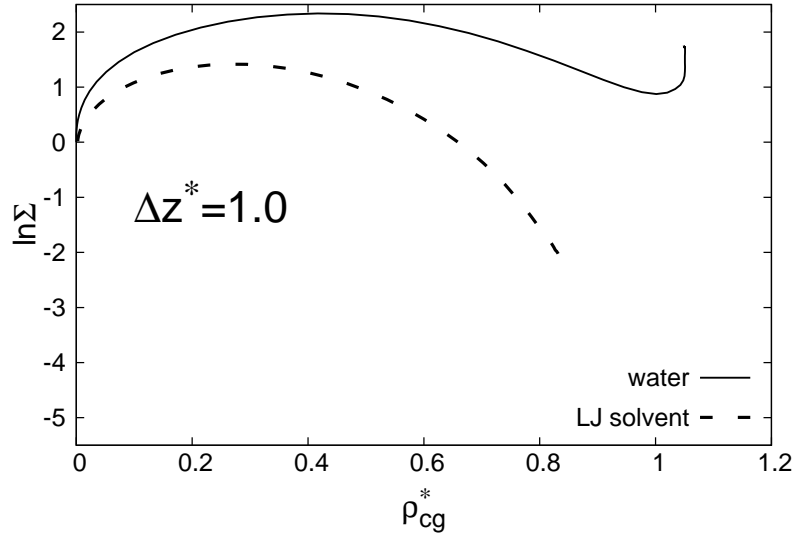


(a)

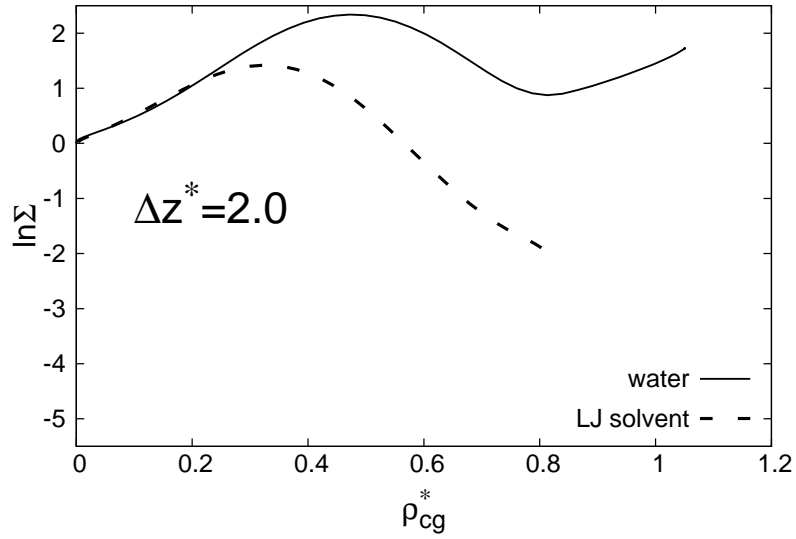


(b)

Figure 2.2: Correlation between $\ln \Sigma$ of the LJ solute and the reduced coarse-grained solvent density ρ_{cg}^* for water (solid line) and the LJ solvent (dashed line). The Δz^* with which ρ_{cg}^* is defined is (a) 1.0 and (b) 2.0. The solute-solvent LJ parameters are $\sigma^* = 1.0$ and $\varepsilon^* = 0.5$ both for water and for the LJ solvent. The temperatures are the same as in Fig. 2.1.



(a)



(b)

Figure 2.3: Correlation between $\ln \Sigma$ of the LJ solute and the reduced coarse-grained solvent density ρ_{cg}^* . The value of ε^* is chosen so that ε^*/T^* is common for the two systems: for water $T^* = 2.929$ ($T = 273\text{K}$) and $\varepsilon^* = 2.09$; for the LJ solvent $T^* = 0.7$ and $\varepsilon^* = 0.50$.

its interface under the condition that σ^* and ε^*/T^* are common for the two systems. This implies that the difference in Σ at given ρ_{cg}^* between water and the LJ solvent is caused by difference in structure of the solvent with its interface. The next question is in what way the structure differs from each other. The viewpoint of the test-particle insertion suggests that there are two different aspects of the solvent structure that may affect the local solubility. The first is the probability of forming a sufficiently large cavity that can accommodate a solute molecule. Note that the Boltzmann factor in Eq. (2.6) is essentially 0 if the repulsive core of a test particle overlaps with any one of repulsive cores of the solvent molecules. The second is the coordination number of solvent molecules around such cavities. The greater the number of solvent molecules in the first solvation shell, the lower the potential energy Ψ in Eq. (2.6) between the test particle and solvent molecules.

Here we focus on the probability of cavity formation by calculating the local solubility of hard-sphere solutes in water and in the LJ solvent, both with their liquid-vapor interfaces. The solute-solvent interaction potential $\phi_{\text{HS}}(r)$ is now

$$\phi_{\text{HS}}(r) = \begin{cases} +\infty & (r < d) \\ 0 & (r \geq d). \end{cases} \quad (2.7)$$

The center of the solute molecule cannot be in any one of the exclusion spheres—the spheres of radius d centered at solvent particles. The solubility Σ of the hard-sphere solute is equal to the probability that the center of the test particle is not included in any one of the exclusion spheres:

$$\Sigma = \frac{V - V_{\text{ex}}}{V}, \quad (2.8)$$

where $V - V_{\text{ex}}$ is the volume not covered by any exclusion spheres and V_{ex} is called the excluded volume. In particular, if d is smaller than half the contact distance d_{BB} between solvent molecules, then V_{ex} is N times the volume of each exclusion sphere and

$$\Sigma = 1 - (4/3)\pi d^3 \rho_{\text{B}}. \quad (2.9)$$

That is, Σ is a function of ρ_{B} alone and is independent of the solvent structure. The condition $d < d_{\text{BB}}/2$ is, however, unrealistic since the center of a solute particle may even penetrate into the

repulsion core of a solvent molecule. Thus, we now consider the case $d > d_{\text{BB}}/2$, where difference in solvent structure does matter in determining Σ of hard-spheres.

For inhomogeneous systems with a liquid-vapor interface, Σ of a hard-sphere depends on z and cannot be evaluated from Eq. (2.8). The local solubility $\Sigma(z)$ is then given by

$$\Sigma(z) = \frac{A - A_{\text{ex}}(z)}{A}, \quad (2.10)$$

where A is the area of the x - y plane at z and $A_{\text{ex}}(z)$ is the area of the intersection of the x - y plane and the exclusion spheres.

In the following paragraph, we examine the correlation between $\Sigma(z^*)$ and $\rho_{\text{cg}}^* = \rho_{\text{cg}} \sigma_{\text{BB}}^3$, the reduced coarse-grained solvent density with $\Delta z^* = d^*$. The values of $d^* = d/\sigma_{\text{BB}}$ are chosen to be common between the two solvents. The solvent-solvent contact distance d_{BB} of water and that of the LJ solvent are defined as the distance that for any $r < d_{\text{BB}}$, the solvent-solvent radial distribution function in the bulk liquid is zero. We find $d_{\text{BB}}^* = d_{\text{BB}}/\sigma_{\text{BB}} = 0.78$ for water and $d_{\text{BB}}^* = 0.92$ for the LJ solvent. For the two solvents, the overlapping of the exclusion spheres may occur when $d^* = 1.0$. We do not consider $d^* < 0.39$ for water and $d^* < 0.46$ for the LJ solvent, for then Σ is expected to be a function of ρ_{cg}^* alone.

In Fig. 2.4, the local solubility Σ of the hard-sphere solute with $d^* = 1.0$ in water and that in the LJ solvent are given as functions of ρ_{cg}^* . For all values of ρ_{cg}^* the solubility of hard-sphere in water is greater than that in the LJ solvent. The same behavior is found for other values of d^* ($= 0.6, 0.7, \dots, 2.0$). That the reduced intermolecular distance r_c/σ_{BB} of the first peak in the solvent-solvent radial distribution function for water is shorter than that for the LJ solvent is consistent with the present result, since the shorter r_c/σ_{BB} , the larger the overlapping volume of the exclusion spheres and the smaller the excluded volume. Recall that when the structure of solvent is the only difference between the two systems, the solubility of the LJ solute in water is higher than that in the LJ solvent (previous subsection). Our result indicates that this is partly because the probability of cavity formation in water is higher than that in the LJ solvent, if the reduced density ρ_{cg}^* is common for the two solvents.

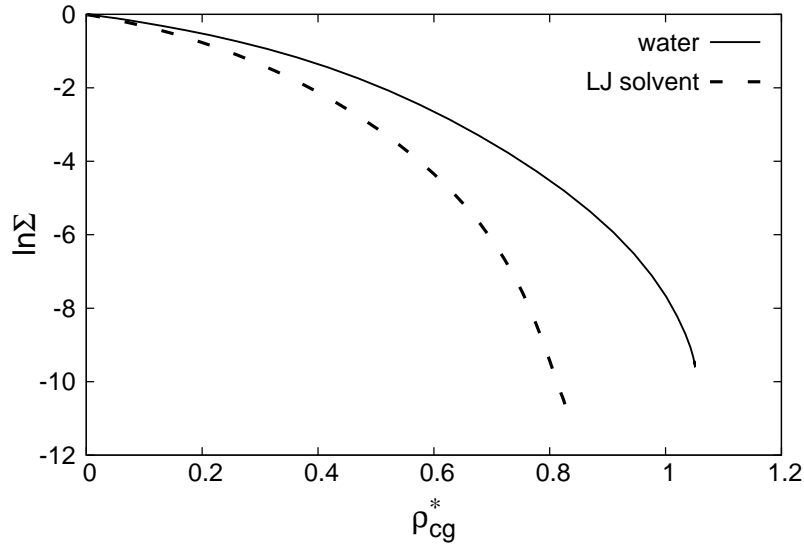


Figure 2.4: Correlation between $\ln \Sigma$ of the hard-sphere solute with $d^* = 1$ and the reduced coarse-grained density ρ_{cg}^* for water (solid line) and for the LJ solvent (dashed line). The local density of the solvent is coarse-grained over $[z^* - d^*, z^* + d^*]$.

Universality in the probability of cavity formation against a scaled density of the solvent

In the previous subsection, we have seen that for a given d^* ($> d_{BB}^*/2$), the probability of cavity formation Σ in water is greater than that in the LJ solvent, provided that the reduced coarse-grained solvent density ρ_{cg}^* is common for the two solvents (Fig. 2.4). Now, we examine the dependence of Σ on a scaled coarse-grained density of the solvent $\rho_{cg}^* = \rho_{cg}/\rho_B^1$, where ρ_B^1 is the bulk liquid density of the solvent. Plotted in Fig. 2.5 is $\ln \Sigma$ of the hard-sphere solute with $d^* = 1.0$ for water and that for the LJ solvent against the scaled density ρ_{cg}^* . The $\ln \Sigma$ vs ρ_{cg}^* curves for the two solvents are much closer to each other than the $\ln \Sigma$ vs ρ_{cg}^* curves in Fig. 2.4. We propose that for a given d^* ($> d_{BB}^*/2$), the probability of forming the cavity in the liquid-vapor interface might be a universal function of the scaled coarse-grained density of the solvent ρ_{cg}^* . At least, from the present study, the universality is observed for the liquid-vapor interface of water and that of simple fluids, when they are close to the triple point.

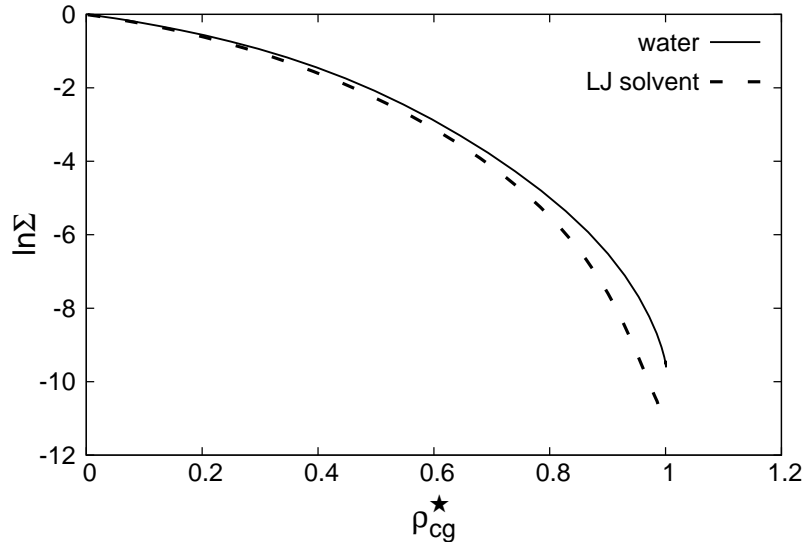


Figure 2.5: Correlation between $\ln \Sigma$ of the hard-sphere solute with $d^* = 1.0$ and the scaled coarse-grained solvent density $\rho_{cg}^* = \rho_{cg}/\rho_B^l$ for water (solid line) and for the LJ solvent (dashed line), where ρ_B^l is the bulk liquid density of each solvent.

References

- [1] V. M. Kaganer, H. Möhwald, and P. Dutta. *Rev. Mod. Phys.*, **71**, 779 (1999).
- [2] K. B. Eisenthal. *Chem. Rev.*, **96**, 1343 (1996).
- [3] G. L. Richmond. *Chem. Rev.*, **102**, 2693 (2002).
- [4] P. Jungwirth and D. J. Tobias. *Chem. Rev.*, **106**, 1259 (2006).
- [5] I. Benjamin. *Acc. Chem. Res.*, **28**, 233 (1995).
- [6] B. C. Garrett, G. K. Schenter, and A. Morita. *Chem. Rev.*, **106**, 1355 (2006).
- [7] T. M. Chang and L. X. Dang. *Chem. Rev.*, **106**, 1305 (2006).
- [8] L. R. Pratt and A. Pohorille. *Chem. Rev.*, **102**, 2671 (2002).
- [9] Y. R. Shen. *Nature*, **337**, 519 (1989).
- [10] J. M. Hicks, K. Kemnitz, K. B. Eisenthal, and T. F. Heinz. *J. Phys. Chem.*, **90**, 560 (1986).

- [11] D. J. Donaldson, J. A. Guest, and M. C. Goh. *J. Phys. Chem.*, **99**, 9313 (1995).
- [12] T. L. Tarbuck and G. L. Richmond. *J. Am. Chem. Soc.*, **127**, 16806 (2005).
- [13] T. L. Tarbuck and G. L. Richmond. *J. Am. Chem. Soc.*, **128**, 3256 (2006).
- [14] G. Ma and H. C. Allen. *Langmuir*, **22**, 5341 (2006).
- [15] T. Rasing, Y. R. Shen, M. W. Kim, P. Valint, Jr., and J. Bock. *Phys. Rev. A*, **31**, 537 (1985).
- [16] E. Tyrode, C. M. Johnson, A. Kumpulainen, M. W. Rutland, and P. M. Claesson. *J. Am. Chem. Soc.*, **127**, 16848 (2005).
- [17] I. Benjamin. *Chem. Rev.*, **96**, 1449 (1996).
- [18] A. Pohorille and I. Benjamin. *J. Chem. Phys.*, **94**, 5599 (1991).
- [19] P. Jedlovszky, I. Varga, and T. Gilányi. *J. Chem. Phys.*, **119**, 1731 (2003).
- [20] L. B. Pártay, P. Jedlovszky, P. N. M. Hoang, S. Picaud, and M. Mezei. *J. Phys. Chem. C*, **111**, 9407 (2007).
- [21] R. Vácha, P. Slavíček, M. Mucha, B. J. Finlayson-Pitts, and P. Jungwirth. *J. Phys. Chem. A*, **108**, 11573 (2004).
- [22] R. Vácha, P. Jungwirth, J. Chen, and K. Valsaraj. *Phys. Chem. Chem. Phys.*, **8**, 4461 (2006).
- [23] R. S. Taylor, D. Ray, and B. C. Garrett. *J. Phys. Chem. B*, **101**, 5473 (1997).
- [24] A. J. Howes and C. J. Radke. *Langmuir*, **23**, 1835 (2007).
- [25] B. Widom. *J. Stat. Phys.*, **19**, 563 (1978).
- [26] B. Widom. *J. Phys. Chem.*, **86**, 869 (1982).
- [27] J. S. Rowlinson and B. Widom. *Molecular theory of capillarity*, page 82. Dover Publications, New York (2002).
- [28] J. O. Hirschfelder, C. F. Curtiss, and R. B. Bird. *Molecular theory of gases and liquids*. Wiley, New York (1954).

- [29] J. L. F. Abascal and C. Vega. *J. Chem. Phys.*, **123**, 234505 (2005).
- [30] C. Ibergay, A. Ghoufi, F. Goujon, P. Ungerer, A. Boutin, B. Rousseau, and P. Malfreyt. *Phys. Rev. E*, **75**, 051602 (2007).
- [31] A. Pohorille and M. A. Wilson. *J. Chem. Phys.*, **104**, 3760 (1996).
- [32] H. A. Patel, E. B. Nauman, and S. Garde. *J. Chem. Phys.*, **119**, 9199 (2003).
- [33] J. S. Rowlinson and B. Widom. *Molecular theory of capillarity*, page 31. Dover Publications, New York (2002).
- [34] B. Hess, C. Kutzner, D. v. d. Spoel, and E. Lindahl. *J. Chem. Theory Comput.*, **4**, 435 (2008).
- [35] S. Nosé. *J. Chem. Phys.*, **81**, 511 (1984).
- [36] S. Nosé. *Mol. Phys.*, **52**, 255 (1984).
- [37] W. G. Hoover. *Phys. Rev. A*, **31**, 1695 (1985).

Chapter 3

Temperature dependence of local solubility of hydrophobic molecules in the liquid-vapor interface of water

3.1 Abstract

One important aspect of the hydrophobic effect is that solubility of small, nonpolar molecules in liquid water decreases with increasing temperature. We investigate here how the characteristic temperature dependence in liquid water persists or changes in the vicinity of the liquid-vapor interface. From the molecular dynamics simulation and the test-particle insertion method, the local solubility Σ of methane in the liquid-vapor interface of water as well as Σ of nonpolar solutes in the interface of simple liquids are calculated as a function of the distance z from the interface. We then examine the temperature dependence of Σ under two conditions: variation of Σ at fixed position z and that at fixed local solvent density around the solute molecule. It is found that the temperature dependence of Σ at fixed z depends on the position z and the system whereas Σ at fixed local density decreases with increasing temperature for all the model solutions at any fixed density between vapor and liquid phases. The monotonic decrease of Σ under the fixed-density condition in the liquid-vapor interface is in accord with what we know for the solubility of nonpolar molecules in bulk liquid water under the fixed-volume condition but it is much robust since the solvent density to be fixed can be anything between the coexisting vapor and liquid phases. A unique feature found in the

water interface is that there is a minimum in the local solubility profile $\Sigma(z)$ on the liquid side of the interface. We find that with decreasing temperature the minimum of Σ grows and at the same time the first peak in the oscillatory density profile of water develops. It is likely that the minimum of Σ is due to the layering structure of the free interface of water.

3.2 Introduction

The solubility of nonpolar gases in liquid water is very small and decreases with increasing temperature T at a fixed pressure. A main question we wish to answer below is how the *local* solubility in the vicinity of the water liquid-vapor interface varies with T or, more simply, whether or not the characteristic temperature dependence of the hydrophobic hydration manifests itself in the interfacial water. To elucidate the solvation of hydrophobic molecules in the water interface we examine similarities and differences in the local solubility between the liquid-vapor interface of water and those of simple fluids.

The solubility Σ of a solute (component A) in a solvent (component B) is here taken to be the ratio of the number density ρ_A of the solute to the activity ζ_A :

$$\Sigma = \rho_A / \zeta_A, \quad (3.1)$$

where ζ_A is related to the chemical potential μ_A by $\zeta_A = \Lambda_A^{-3} \exp(\mu_A/kT)$ with Λ_A the thermal de Broglie wavelength of species A and k the Boltzmann constant. When the solution is in equilibrium with a dilute gas of A, Σ is the Ostwald absorption coefficient. Since the excess chemical potential μ_{ex} is a logarithmic measure of Σ :

$$\mu_{\text{ex}} = -kT \ln \Sigma, \quad (3.2)$$

the low solubility ($\Sigma \ll 1$) is characterized by a large positive value of μ_{ex} . The decrease of Σ with temperature means $[\partial(\mu_{\text{ex}}/T)/\partial(1/T)]_p < 0$ and the latter in turn indicates that the solvation at fixed pressure is exothermic, provided that the coefficient of thermal expansion α_p is sufficiently small or negative. To explain the energetically favorable and entropically unfavorable solvation, Frank and Evans proposed the iceberg model in 1945 [1], and since then much effort has been devoted to explain a microscopic origin of this tendency [2–10]; however, it has been pointed

out from purely thermodynamic arguments that the solvation enthalpy and the solvation entropy depend on a choice of thermodynamic conditions: fixed pressure, fixed volume, or an arbitrary volume-change condition [11]. For example, the difference between the solvation enthalpy h_p in the constant-pressure process and the solvation energy u_v in the fixed-volume process is $T\gamma_V v_p$, with $\gamma_V = (\partial p/\partial T)_V$ the thermal pressure coefficient of the solution and v_p the partial molecular volume of solute. For most solutes and solvents, the difference is not small compared to kT . For water, however, γ_V is very small near the triple point and becomes zero at 4°C. Thus the difference $(h_p - u_v)/kT$ for aqueous solutions is unusually small at low temperatures. There is no reason to assume that the thermodynamic condition in which the temperature dependence of μ_{ex} is evaluated is less important for the solvation in the liquid-vapor interface. But so far the temperature dependence of the local solubility or the excess chemical potential has not been examined with particular attention to the thermodynamic condition.

Microscopic and macroscopic properties of solutes in the water interface, such as molecular orientation [12, 13] and phase transitions [14–17], are probed by surface specific spectroscopy, e.g., second harmonic [18] and sum-frequency generation [19] spectroscopy. It is, however, very difficult to investigate by experiment the local solubility $\Sigma(z)$ or the excess chemical potential $\mu_{\text{ex}}(z)$ of hydrophobic molecules in the water interface as a function of z the coordinate perpendicular to the interface. Computer-simulation and theoretical studies are thus far the only practical method to examine this problem [20–27]. Notable features observed for $\mu_{\text{ex}}(z)$ of nonpolar solutes in the water interface are the following: (i) $\mu_{\text{ex}}(z)$ has a minimum in the interfacial region, i.e., solutes are surface active and (ii) $\mu_{\text{ex}}(z)$ has a maximum at a small distance away from the position of minimum to the liquid side, i.e., there is a free-energy barrier between the adsorbed region and the bulk liquid region. It has yet to be examined whether (i) and (ii) are characteristic of the hydrophobic hydration in the water interface or can be observed for solvation in other interfaces.

In this article, we study the liquid-vapor interfaces of a model aqueous solution of methane (denoted by methane/water), a model krypton solution of methane (methane/krypton), and a hypothetical LJ solution (hydrophobic LJ/LJ). The methane/water and the hydrophobic LJ/LJ systems exhibit $\mu_{\text{ex}} > 0$ and $h_p < 0$ in the liquid state near the triple point whereas methane/krypton shows $\mu_{\text{ex}} < 0$ and $h_p < 0$ in the bulk liquid. What is to be obtained is the local solubility $\Sigma(z) = \exp[-\mu_{\text{ex}}(z)/kT]$ and its temperature dependence in the nonuniform fluids at the liquid-vapor coexistence. The quan-

tity $\Sigma(z)$ is proportional to the local number density $\rho_A(z)$ of the solute species, or more precisely it is the ratio of $\rho_A(z)$ to the activity of the solute. Calculation of $\Sigma(z)$ is implemented by a standard method of molecular simulation: First, we obtain equilibrium structures of a pure solvent in the liquid-vapor equilibrium by the canonical-ensemble molecular dynamics (MD) simulation and then we carry out the test-particle insertion of a solute particle in the equilibrium configurations.

The thermodynamic states examined are those along the liquid-vapor coexistence curve including a metastable extension beyond the triple point. This is the macroscopic condition of the temperature variation, in which neither the pressure nor the density of each phase is fixed. Thus it seems impossible to examine temperature dependences of Σ under different conditions as we have done in the bulk liquid [11]. There is, however, a variety of microscopic conditions. A natural choice among them is the fixed- z condition, in which the temperature dependence of Σ at given z is examined. Another choice is the fixed-density condition, in which variation of Σ at a fixed local solvent density with varying temperature is evaluated. We will present and discuss the temperature dependences of the local solubility in the fixed- z and fixed-density conditions for the methane/water, methane/krypton, and hydrophobic LJ/LJ systems.

In section 3.3, we review the potential distribution theorem for nonuniform solutions, a theoretical basis for the calculation of Σ . The model systems and the method of computation are described in Sec. 3.4 and 3.5, respectively. We then present results and discussion in Sec. 3.6 followed by a brief summary in Sec. 3.7.

3.3 Theoretical background

Following the original derivation of the uniformity of the chemical potential in a nonuniform fluid [28], we review the theoretical basis of the calculation of the local solubility of a solute species in a nonuniform fluid. Suppose a solution of N_A solute and N_B solvent molecules to be in the liquid-vapor coexistence at temperature T in a box of volume V .

As a generalization of Eq. (1), one may define the local solubility $\Sigma(\mathbf{r})$ of solute A at a position \mathbf{r} by

$$\Sigma(\mathbf{r}) = \frac{\rho_A(\mathbf{r})}{\zeta_A}, \quad (3.3)$$

where $\rho_A(\mathbf{r})$ is the local number density of A at \mathbf{r} and ζ_A is the activity of A as in Eq. (1). Note

that the uniformity of activity of each species in an inhomogeneous fluid, though not self-evident, can be shown by the potential distribution theorem [28]. When \mathbf{r} is in a liquid region far away from the liquid-vapor interface, $\Sigma(\mathbf{r})$ is much smaller than 1 for aqueous solutions of hydrophobic molecules; when \mathbf{r} is in a vapor phase $\Sigma(\mathbf{r}) \simeq 1$. The excess chemical potential is related to $\Sigma(\mathbf{r})$ as in Eq. (2): $\mu_{\text{ex}}(z) = -kT \ln \Sigma(z)$.

From the Boltzmann distribution law, the local number density $\rho_A(\mathbf{r})$ of solute A at \mathbf{r} is

$$\rho_A(\mathbf{r}) = N_A \int \dots \int \frac{e^{-U_N(\mathbf{r}, \mathbf{r}_2, \dots, \mathbf{r}_N)/kT}}{Q_N} d\mathbf{r}_2 \dots d\mathbf{r}_N, \quad (3.4)$$

where U_N is the potential energy of the system in the configuration $\mathbf{r}, \mathbf{r}_2, \dots, \mathbf{r}_N$ with $N = N_A + N_B$ and the first N_A \mathbf{r} 's being those of the solute molecules and Q_N is the configuration integral. The potential energy U_N can be divided into two parts:

$$U_N = U_{N-1} + \Phi(\mathbf{r}), \quad (3.5)$$

where U_{N-1} is the potential energy of the system in the same configuration except that the solute molecule at \mathbf{r} is absent and $\Phi(\mathbf{r})$ is the potential energy change due to the presence of the solute molecule at \mathbf{r} . With this $\Phi(\mathbf{r})$,

$$\rho_A(\mathbf{r}) = N_A \frac{Q_{N-1}}{Q_N} \langle e^{-\Phi(\mathbf{r})/kT} \rangle, \quad (3.6)$$

where Q_{N-1} is the configuration integral of the system of $(N_A - 1)$ solute molecules and N_B solvent molecules and $\langle e^{-\Phi(\mathbf{r})/kT} \rangle$ is the average of $e^{-\Phi(\mathbf{r})/kT}$ with the factor of $\exp(-U_{N-1}/kT)/Q_{N-1}$. The quantity $N_A Q_{N-1}/Q_N$ is independent of \mathbf{r} and may be identified with the activity ζ_A since it is the activity when the system is uniform. Then the local solubility $\Sigma(\mathbf{r})$ is expressed as

$$\rho_A(\mathbf{r})/\zeta_A = \langle e^{-\Phi(\mathbf{r})/kT} \rangle. \quad (3.7)$$

When the solution is nonuniform in the z direction alone, $\Sigma(\mathbf{r}) = \Sigma(z)$. Furthermore, when the solution is infinitely dilute in A, the right-hand side of Eq. (3.7) is the average over the configuration of N_B solvent molecules. With these conditions the local solubility $\Sigma(z)$ in the model solutions of

methane/water, methane/krypton, and hydrophobic LJ/LJ is obtained by the test-particle insertion, which evaluates the right-hand side of Eq. (3.7). Details of the calculation are described in Sec. 3.5.

3.4 Model systems

The three model solutions, which are all infinitely dilute, are methane/water, methane/krypton, and hydrophobic LJ/LJ. The intermolecular interaction for pure water is of the TIP4P/2005 model [29] and the methane-water interaction is taken to be the LJ potential between the oxygen site of water and the united-atom site of methane with the parameters given by the Lorentz-Berthelot rule. The intermolecular interactions for the other two systems are all LJ potentials. The solute-solvent LJ parameters for methane/krypton are those derived from the parameter sets for methane and krypton [30] by the Lorentz-Berthelot rule. The solute-solvent LJ parameters for hydrophobic LJ/LJ is chosen such that $\mu_{\text{ex}} > 0$ and $h_p < 0$ in the LJ liquid near the triple point. The LJ parameters σ_{BB} , ε_{BB} of the solvent-solvent interaction and σ_{AB} , ε_{AB} of the solute-solvent interaction for the three model systems are listed in Table 3.1.

It is instructive to review when μ_{ex} and h_p of LJ solutions are those characteristic of hydrophobic hydration, i.e., $\mu_{\text{ex}} > 0$ and $h_p < 0$ and when they are not. In principle the thermodynamic character of solvation can be classified into four types by the signs of μ_{ex} and h_p : $\mu_{\text{ex}} < 0$ and $h_p < 0$, $\mu_{\text{ex}} < 0$ and $h_p > 0$, $\mu_{\text{ex}} > 0$ and $h_p < 0$, and $\mu_{\text{ex}} > 0$ and $h_p > 0$. Figure 3.1 is the “solvation diagram” for the LJ solution at infinite dilution near the triple point ($T^* = kT/\varepsilon_{\text{BB}} = 0.7$ and $\rho_{\text{B}}^* = \rho_{\text{B}}\sigma_{\text{BB}}^3 = 0.8507$) [11]. The diagram shows domains of the four types of solvation in the $\sigma_{\text{AB}}^* - \varepsilon_{\text{AB}}^*$ plane, where $\sigma_{\text{AB}}^* = \sigma_{\text{AB}}/\sigma_{\text{BB}}$ and $\varepsilon_{\text{AB}}^* = \varepsilon_{\text{AB}}/\varepsilon_{\text{BB}}$, and data points corresponding to various combinations of nonpolar solutes and nonpolar solvents. In the domain of $\mu_{\text{ex}} < 0$ and $h_p < 0$ there are the methane/krypton solution and other solutions that the size of the solute molecule is similar to or larger than that of the solvent molecule and the solute-solvent attractive interaction is similar to or stronger than the solvent-solvent one. There are no data points of real solutions in the domain of $\mu_{\text{ex}} < 0$ and $h_p > 0$. The shaded region indicates the domain of $\mu_{\text{ex}} > 0$ and $h_p < 0$, i.e., of the hydrophobic-hydration type. The region is so narrow that only He/Ne among the list of solutions falls in this region. The parameter set for the hydrophobic LJ/LJ, which is close to that of He/Ne, is chosen from this hydrophobic domain. In the region of $\mu_{\text{ex}} > 0$ and $h_p > 0$, where the solubility

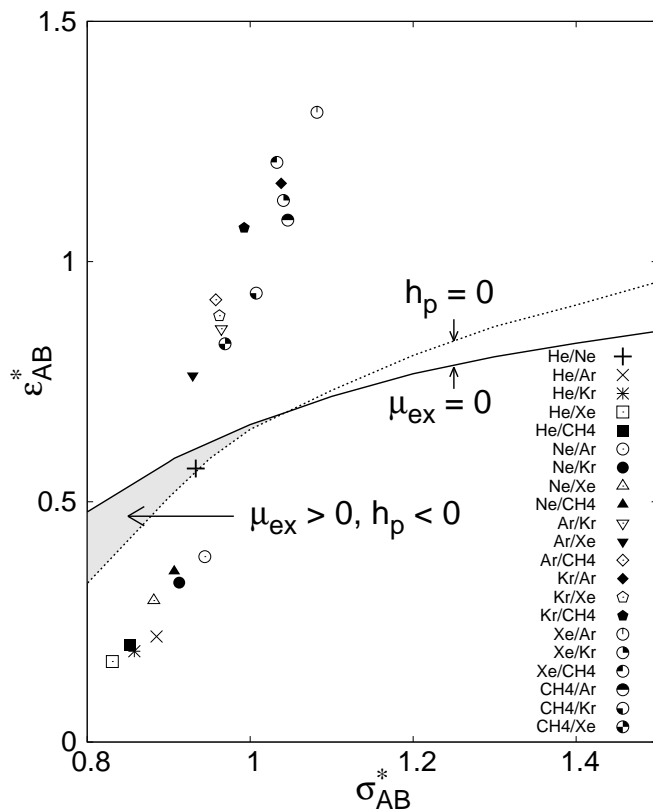


Figure 3.1: Solvation diagram for the LJ solution on the plane of dimensionless solute-solvent LJ parameters, ϵ_{AB}^* , σ_{AB}^* . The locus of $\mu_{ex} = 0$ (solid line) and that of $h_p = 0$ (dotted line) are obtained at the temperature $k_B T / \epsilon_{BB} = 0.7$ and the solvent density $\rho \sigma_{BB}^3 = 0.8507$ in Ref. [11]. The shaded region indicates the domain of hydrophobic solvation ($\mu_{ex} > 0$, $h_p < 0$). Symbols correspond to sets of LJ parameters for real solutions of nonpolar solutes and solvents.

is low and the solvation is energetically unfavorable, one finds many data points such as He/Ar, He/Kr, He/Xe, Ne/Ar, Ne/Kr, and Ne/Xe. These are combinations of small solute and large solvent molecules.

3.5 Method

The local solubility $\Sigma(z)$ in the liquid-vapor interface of the model solutions is calculated by the test-particle insertion method, the theoretical background of which is described in Sec. 3.3. Equilibrium configurations of pure solvents in the liquid-vapor equilibria, in which test particles are inserted, are obtained by the canonical-ensemble (*NVT*) MD simulation with the Nosé [31] or Nosé-Hoover thermostat [32, 33].

System	Solvent-solvent	σ_{BB}	$\varepsilon_{\text{BB}}/k$	Solute-solvent	$\sigma_{\text{AB}}/\sigma_{\text{BB}}$	$\varepsilon_{\text{AB}}/\varepsilon_{\text{BB}}$
methane/water	TIP4P/2005	3.1589	93.2	LJ	1.090	1.2599
methane/krypton	LJ	3.675	169.0	LJ	1.007	0.9342
hydrophobic LJ/LJ	LJ	—	—	LJ	0.900	0.5600

Table 3.1: Potential models for solvent-solvent and solute-solvent pair interactions and their LJ parameters. The solvent-solvent LJ parameters σ_{BB} and $\varepsilon_{\text{BB}}/k$ are in units of Å and K, respectively. The solute-solvent parameters σ_{AB} , ε_{AB} of methane/water and methane/krypton are determined by the Lorentz-Berthelot rule with LJ parameters of each species. [30]. For the hydrophobic LJ/LJ, $\sigma_{\text{AB}}/\sigma_{\text{BB}}$ and $\varepsilon_{\text{AB}}/\varepsilon_{\text{BB}}$ are chosen from the domain of hydrophobic solvation where $\mu_{\text{ex}} > 0$ and $h_p < 0$ in the LJ liquid (see Fig. 3.1).

In the simulation of water, 1372 molecules are confined in a rectangular box ($L_x = L_y = 37.15$ Å, $L_z = 111.5$ Å) with the periodic boundary conditions applied in the three directions. The initial configuration is prepared by placing a dense liquid slab at the middle of the rectangular box such that its interfaces are normal to the z direction. The MD simulations are performed by using the program package GROMACS (version 4.5.5): the time step is 1 fs, the Coulomb interactions are treated by the particle mesh Ewald method, and both the Coulomb and LJ interaction potentials are smoothly truncated by a switching function between 12 and 13 Å. After the equilibration period of 10^6 steps (1 ns), the configurations are recorded every 100 steps.

The simulation of the LJ fluid is carried out in the same manner as that of water. The number of particles are 1372 and the box dimensions are $L_x = L_y = 11.76\sigma_{\text{BB}}$, $L_z = 35.29\sigma_{\text{BB}}$. The LJ interaction is gradually truncated by a switching function between $3.91\sigma_{\text{BB}}$ and $4.50\sigma_{\text{BB}}$. These conditions are comparable to those used in the previous studies [34–36]. The numerical integration is implemented by our MD simulation program. After the equilibration run (10^6 steps) the configurations are sampled every 100 steps.

The test-particle insertion is performed for $6 \times 10^5 - 80 \times 10^5$ equilibrium configurations of each model solution to calculate the average quantity in Eq. (3.7). As in a previous study [37], the solute molecule is inserted at 70×70 grid points on each of the planes with $z = \text{constant}$. The grid interval is $0.168 \sigma_{\text{BB}}$ and the interval between two planes is $0.1 \sigma_{\text{BB}}$. In total, the number of trial insertions for each plane at given z ranges from 3×10^9 to 40×10^9 , depending on the system and distance z . Then a further average is taken over two liquid-vapor interfaces in each configuration. With the

averaging procedure described here we obtain $\Sigma(z)$ over a range $-4\sigma_{\text{BB}} \leq z \leq 4\sigma_{\text{BB}}$.

When we calculate the equilibrium structure of the liquid-vapor interface of solvents and the local solubility $\Sigma(z)$ of solutes from the instantaneous configurations given by MD simulations, we remove the effect of translational motion of the interface and then obtain the interface structure and $\Sigma(z)$. This is because the liquid slab in the simulation box exhibits the translational motions, even when the total momentum of the whole system is kept zero. The motion of the liquid slab is due to the corresponding opposite motion of molecules in the gas phase, although the two parts of the system together have zero momentum, and thus becomes significant when the number density in the gas phase is high. For example, for the LJ fluid at $T^* = 0.7$, ρ_{B}^* in the gas phase is ~ 0.002 and the position of the equimolar surface moves by more than σ_{BB} over a few nano seconds. In such cases, averaging over a long time with a fixed origin of z leads to unnecessary broadening of the density profile. To avoid this, we divide the whole trajectory of 40×10^5 steps into blocks of 10^5 steps. Then for each block we obtain the equimolar dividing surface and take that position to be $z = 0$. The length of each block is sufficiently long to calculate the dividing surface, and sufficiently shorter than the time scale of the translational motion of the interface. We confirmed that the density profile of solvent molecules for different blocks coincided with each other. In the particle insertion calculation, too, the origin of z defined for each block is employed to remove the effect of the translational motion on $\Sigma(z)$.

3.6 Results

Density profiles of the model water and the LJ fluid

The density profiles $\rho_{\text{B}}(z)$ of the model water and the LJ fluid at various temperatures are shown in Fig. 3.2. The vapor side of the interface is $z < 0$ and the liquid side is $z > 0$. Here and afterwards the local number density of the solvent and the distance from the dividing surface are expressed by the dimensionless quantities $\rho_{\text{B}}^* = \rho_{\text{B}}\sigma_{\text{BB}}^3$ and $z^* = z/\sigma_{\text{BB}}$ with σ_{BB} in Table 3.1. The local density $\rho_{\text{B}}^*(z^*)$ is the average over a bin of $[z^* - 0.05, z^* + 0.05]$.

In the interfacial water, ρ_{B}^* varies rapidly between $z^* \simeq -1$ and $z^* \simeq 1$. As temperature is decreased, not only the interface becomes sharper but also oscillations in $\rho_{\text{B}}^*(z^*)$ on the liquid side appear at 313 K and become pronounced with further cooling down to the supercooled state at

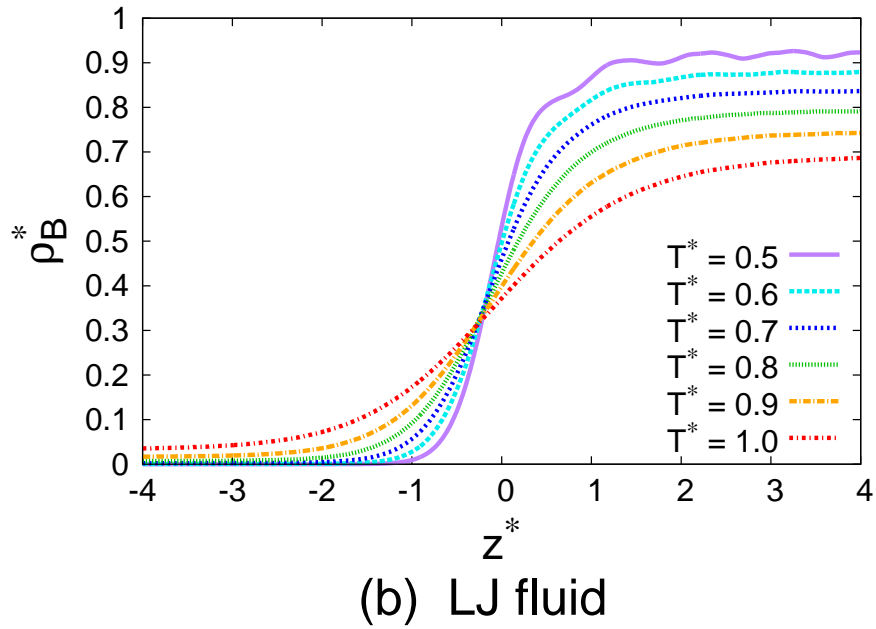
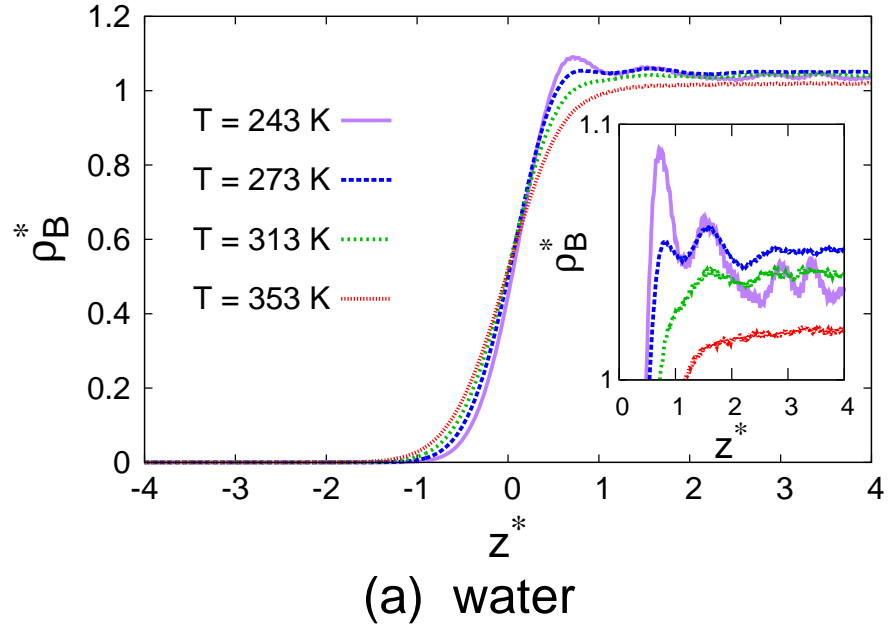


Figure 3.2: Density profiles of (a) the model water and (b) the Lennard-Jones fluid. The density ρ_B^* and the coordinate z^* are dimensionless quantities $\rho_B \sigma_{BB}^3$ and z/σ_{BB} , respectively. The origin $z^* = 0$ is the Gibbs' equimolar surface. The inset in (a) shows surface layering in the water interface.

243 K. The maximum in the density profile has been reported by Wang et al. [38] and the layering structure of the liquid-vapor interface of water has been suggested [39, 40] and clearly revealed by Willard and Chandler [41].

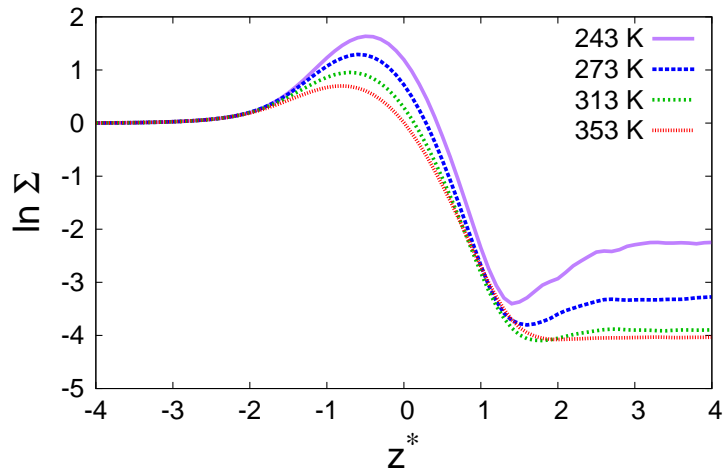
For the LJ fluid, ρ_B^* varies slowly with z^* compared to $\rho_B^*(z^*)$ of water. Much of the change from the gas to the liquid density occurs between $z^* \simeq -2$ and $z^* \simeq 2$ and ρ_B^* still increases very slowly with z for $z^* > 2$. Layering structure of the liquid-vapor interface has been studied for simple fluids in connection with the capillary wave theory [42–44]. Here we find oscillatory behavior in the LJ fluid at metastable liquid-vapor equilibrium states ($T^* = 0.5$ and 0.6).

At the lowest temperature of water the first peak in $\rho_B(z)$ from the interface is highest while at the lowest temperature of the LJ fluid a shoulder, instead of a peak, is found near the equimolar surface.

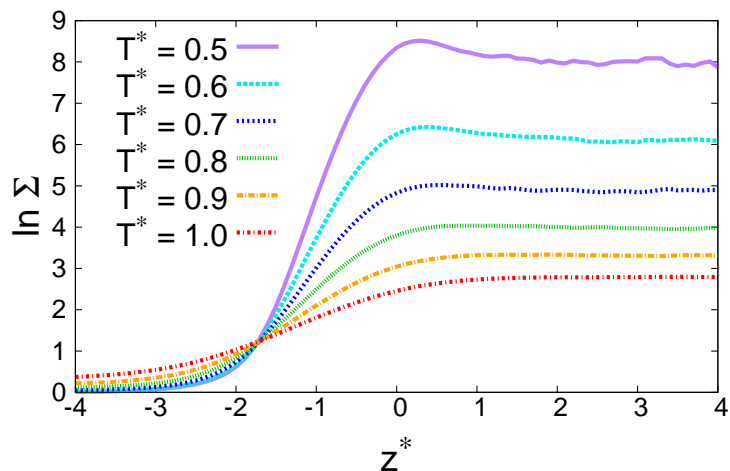
Local solubility as a function of the distance from the interface and its temperature dependence

In Fig. 3.3 we show the logarithm of the local solubility, $\ln \Sigma(z) = -\mu_{\text{ex}}(z)/kT$, for the three systems: methane/water, methane/krypton, and hydrophobic LJ/LJ. Let us first examine the form of $\ln \Sigma(z)$ near the triple point of each solvent. The functions $\ln \Sigma(z)$ for methane/water ($T = 273$ K), methane/krypton ($T^* = 0.7$), and hydrophobic LJ/LJ ($T^* = 0.7$) share a common behavior on the vapor side: as approaching the liquid side from the vapor side, $\ln \Sigma$ increases and then reaches a maximum. The maximum in $\ln \Sigma(z)$ (equally, the minimum in $\mu_{\text{ex}}(z)$) indicates the interface adsorption of solute molecules. However, $\ln \Sigma(z)$ varies in different manners on the liquid side ($z^* > 0$). For methane/water, $\ln \Sigma$ drops to a negative value with increasing z^* . On the other hand, $\ln \Sigma$ for methane/krypton decreases only slightly and approaches a positive value in the liquid phase.

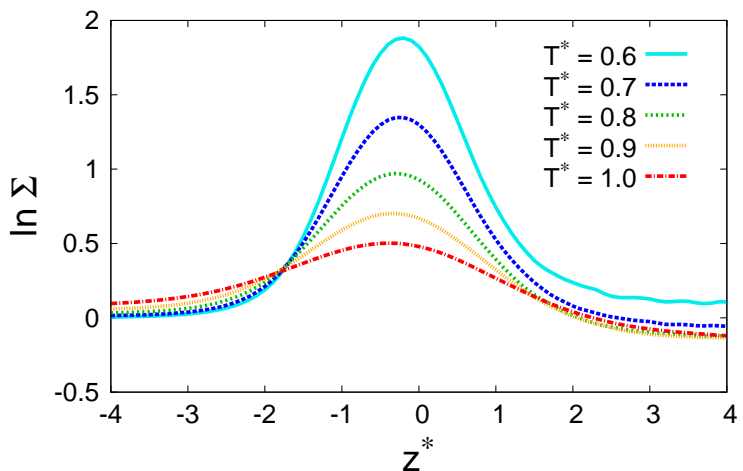
A notable feature uniquely observed for the water interface is that there is a minimum of the local solubility on the liquid side of the interface. The existence of a minimum or a free energy barrier has been reported for other aqueous solutions [20, 23, 27, 45]. At 273 K, the minimum value of Σ at $z^* \simeq 1.2$ is 0.022 while Σ at $z^* = 4$, deep inside the liquid region, is 0.038. The difference between Σ at its minimum and that in the bulk liquid becomes larger with decreasing temperature. At 243 K, the minimum value of Σ is 0.033 and Σ at $z^* = 4$ is 0.1. This tendency is correlated with the growth of the maximum in the local density $\rho_B(z)$ of water with decreasing temperature. Also



(a) methane/water



(b) methane/krypton



(c) hydrophobic LJ/LJ

Figure 3.3: The local solubility Σ as a function of z^* for (a) methane/water, (b) methane/krypton, and (c) hydrophobic LJ/LJ.

we know that the solubility of methane in bulk water decreases with increasing the solvent density at fixed T . Thus it is likely that the minimum in Σ at about one molecular diameter distant from the equimolar surface is mainly caused by the local maximum of the solvent density near the interface.

For hydrophobic LJ/LJ, $\ln \Sigma$ changes its sign from positive to negative with increasing z^* from the maximum, as is the case of methane/water. This is not surprising because we have chosen the solute-solvent LJ parameters from the hydrophobic domain in the solvation diagram in Fig. 3.1. However no minimum in Σ is observed in the range of z examined. We also note the large difference in $\Sigma(z)$ between methane/krypton and hydrophobic LJ/LJ. This means that the effect of the solute-solvent LJ parameters on $\Sigma(z)$ is large in the LJ solvent near the triple point; the effect on $\Sigma(z)$ is much smaller in the water interface near the triple point because the triple point of water is high and so the solute-solvent interaction energy divided by kT is small. [27]

The temperature effect on $\ln \Sigma(z)$ for methane/water is larger in the liquid side ($z^* = 4$) of the interface than at the position of adsorption ($z^* \simeq 0$). This is a notable feature for methane/water; the temperature effect is largest at around $z^* = 0$ for methane/krypton and hydrophobic LJ/LJ. Otherwise the temperature effect on $\ln \Sigma(z)$ is common for all the three systems. The higher the temperature the more gradually $\ln \Sigma$ varies with z^* , which is consistent with the temperature dependence of $\rho_B(z)$ shown in Fig. 3.2. The maximum value of Σ decreases with increasing temperature, i.e., the ratio of the concentration of solute molecules adsorbed at the interface to that in the gas phase decreases with increasing temperature. The profile $\ln \Sigma(z)$ on the vapor side ($z^* \lesssim -2$) weakly depends on T (methane/krypton and hydrophobic LJ/LJ) or is nearly independent of T (methane/water).

Temperature dependence of the local solubility at fixed position

Here we examine the temperature dependence of Σ at three positions, $z^* = -4$ (on the vapor side), $z^* = 0$ (at the equimolar surface), and $z^* = 4$ (on the liquid side). The variations of $\ln \Sigma$ with T are plotted in Fig. 3.4. A common feature for the three systems is that $\ln \Sigma$ on the vapor side is only weakly dependent on T and slightly increases with T . For methane/water one cannot see any deviation from $\ln \Sigma = 0$ in Fig. 3.3a but in fact it increases monotonically with T . The slight increase of Σ is due to the increase of the attractive interaction between a solute molecule and solvent molecules. Thus, as long as the solute-solvent interaction potential has an attractive part,

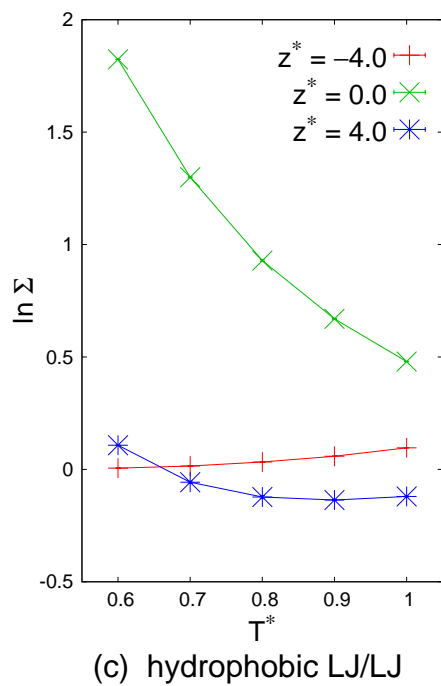
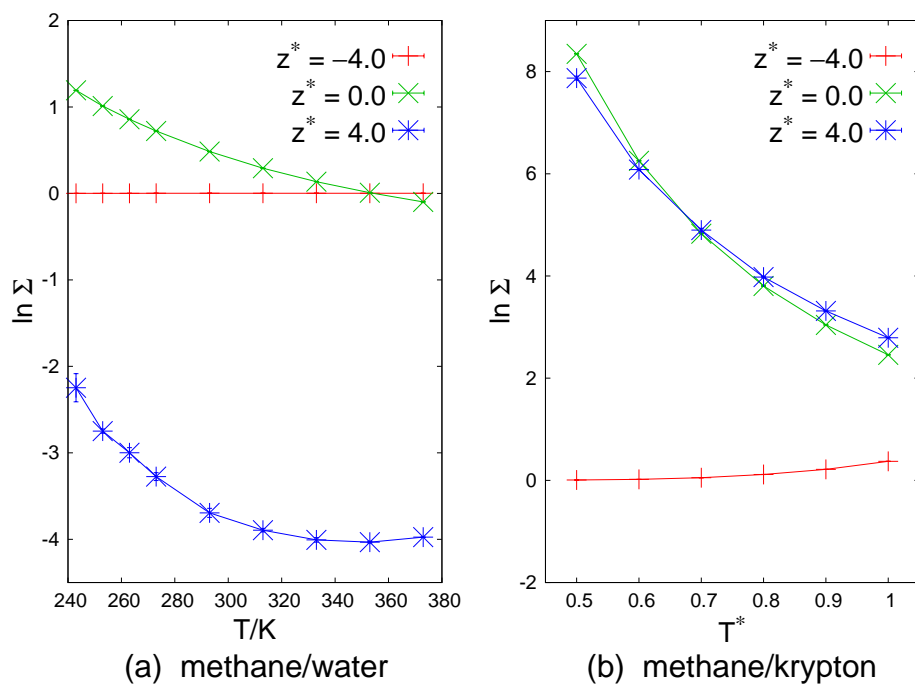


Figure 3.4: Temperature dependence of $\ln \Sigma$ at fixed z^* for (a) methane/water, (b) methane/krypton, and (c) hydrophobic LJ/LJ. There are three choices of z^* : $z^* = -4$ (on the side of vapor phase), $z^* = 0$ (equimolar surface), and $z^* = 4$ (on the side of liquid phase).

the behavior of Σ on the vapor side of the equimolar surface would be qualitatively the same for many combinations of solute and solvent species. At the equimolar surface ($z^* = 0$), $\ln \Sigma$ decreases monotonically with temperature. This is also common for the three systems.

On the liquid side ($z^* = 4$), variation of $\ln \Sigma$ with T depends strongly on the system. For methane/water, $\ln \Sigma$ decreases with T , and then turns to increase around 350 K. The same trend can be found in the isobaric temperature dependence of the Ostwald adsorption coefficient [46, 47] or μ_{ex} [48, 49] of methane in bulk water. For methane/krypton, $\ln \Sigma$ decreases monotonically but the sign of $\ln \Sigma$ remains to be positive. For hydrophobic LJ/LJ, the variation of $\ln \Sigma$ with T exhibits not only a monotonic decrease at low temperatures but also a minimum at a higher temperature. This behavior is qualitatively the same as that for methane/water. In the case of methane/water, however, the local solubility Σ is less than 1 (low solubility) at a position less than one molecular diameter away from the equimolar surface while Σ of hydrophobic LJ/LJ becomes less than 1 at distances of two or three molecular diameters. This indicates that the solvation of methane in water is of hydrophobic character right up to the liquid-vapor interface.

Local solubility as a function of the coarse-grained solvent density

In this section, we examine the correlation between the local solubility and the solvent density around the solute molecule. For this purpose, we introduce a coarse-grained solvent density $\rho_{\text{cg}}(z^*)$, which is defined as the local density $\rho_{\text{B}}^*(z^*)$ averaged over a range of $2\sigma_{\text{AB}}^*$ centered at z^* , and examine the locus of the point $[\ln \Sigma(z^*), \rho_{\text{cg}}(z^*)]$ as z^* is varied from -4 to $+4$. Figure 3.5 shows such isotherms for (a) methane/water, (b) methane/krypton, and (c) hydrophobic LJ/LJ. For methane/water and hydrophobic LJ/LJ, $\ln \Sigma$ decreases with ρ_{cg} for a wide range of ρ_{cg} and becomes negative at large ρ_{cg} , while $\ln \Sigma$ of methane/krypton increases for a wide range of ρ_{cg} and remains to be positive.

The $\ln \Sigma - \rho_{\text{cg}}$ isotherms in Fig. 3.5a-c do not intersect with each other, which is well contrasted with the $\ln \Sigma(z^*) - z^*$ isotherms in Fig. 3.3. Also, as illustrated by the arrows in those figures, the local solubility Σ decreases with increasing temperature at any fixed value of ρ_{cg} . Plotted in Fig. 3.5 are $\ln \Sigma$ at three selected values of $\rho_{\text{cg}}(z^*)$ as functions of temperature. For methane/water (Fig. 3.5d), ρ_{cg} is fixed at $\rho_{\text{cg}}(z^* = -4) = 0.00023$, $\rho_{\text{cg}}(z^* = 0) = 0.5148$, and $\rho_{\text{cg}}(z^* = 4) = 1.0041$ of water at $T=373$ K. For methane/krypton (Fig. 3.5e) and hydrophobic LJ/LJ (Fig. 3.5f), ρ_{cg} is fixed at $\rho_{\text{cg}}(z^* = -4) = 0.0362$, $\rho_{\text{cg}}(z^* = 0) = 0.3670$, and $\rho_{\text{cg}}(z^* = 4) = 0.6853$ of the LJ fluid at

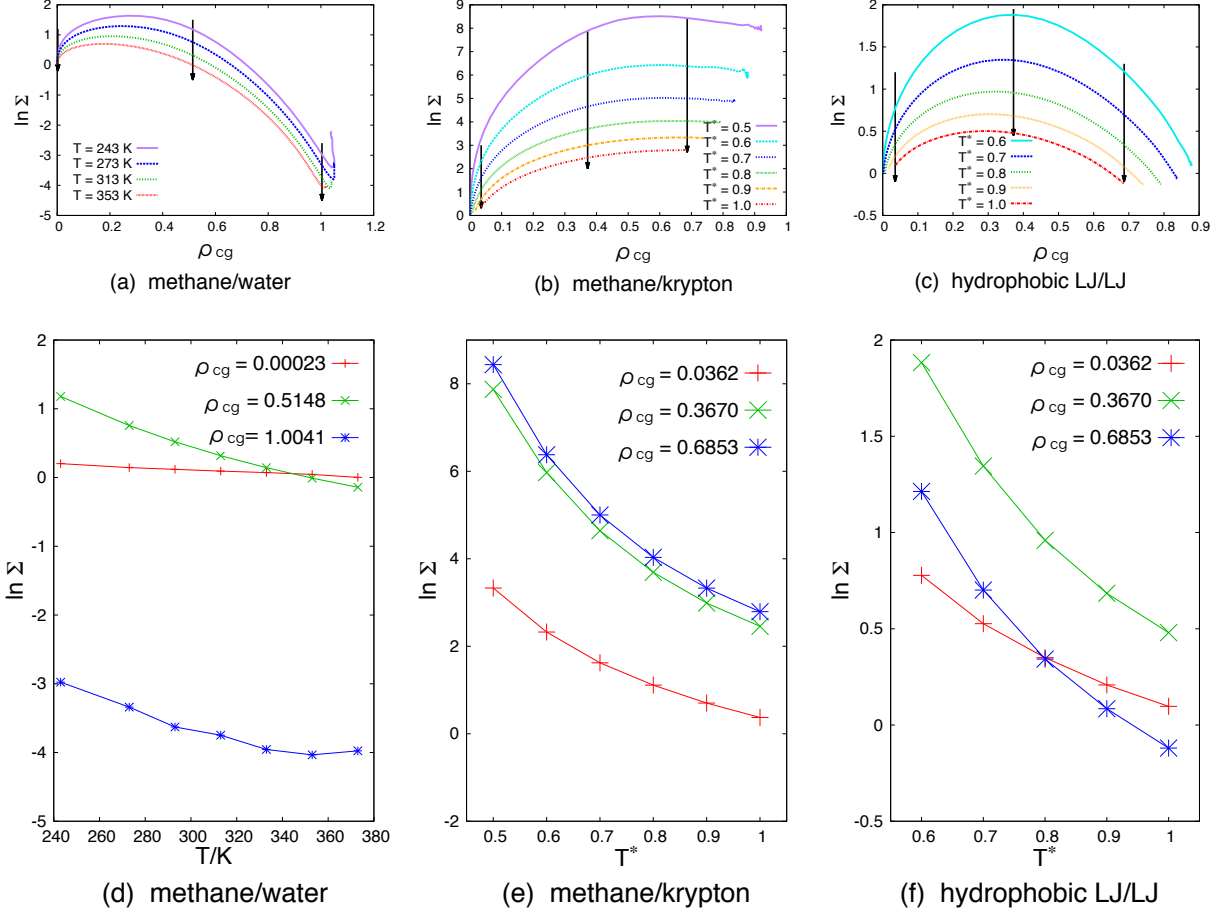


Figure 3.5: Logarithm of local solubility Σ as a function of the coarse-grained solvent density ρ_{cg} for (a) methane/water, (b) methane/krypton, and (c) hydrophobic LJ/LJ. The coarse-grained solvent density $\rho_{cg}(z^*)$ is the average of $\rho_B^*(z^*)$ over $[z^* - \sigma^*, z^* + \sigma^*]$. Each isotherm is a locus of $(\ln \Sigma(z^*), \rho_{cg}(z^*))$ with varying z^* from -4 to 4 . For each system [(d) methane/water, (e) methane/krypton, and (f) hydrophobic LJ/LJ], $\ln \Sigma$ is plotted against the temperature at three fixed values of ρ_{cg} . The three values of ρ_{cg} , which are shown as arrows in (a)-(c), are $\rho_{cg}(z^* = -4) = 0.00023$, $\rho_{cg}(z^* = 0) = 0.5148$, and $\rho_{cg}(z^* = 4) = 1.0041$ of water at $T=373$ K for methane/water and $\rho_{cg}(z^* = -4) = 0.0362$, $\rho_{cg}(z^* = 0) = 0.3670$, and $\rho_{cg}(z^* = 4) = 0.6853$ of the LJ fluid at $T^*=1.0$ for methane/krypton and hydrophobic LJ/LJ.

$T^* = 1.0$. The monotonic decrease of Σ with increasing T at the low, medium, and high density ρ_{cg} is again confirmed here. On the other hand, as we have seen in Fig. 3.4, when z^* is fixed at the vapor side of the interface, Σ slightly increases with T for all the systems; when z^* is fixed at the liquid side Σ decreases with T and then reaches a minimum at a high temperature for methane/water and hydrophobic LJ/LJ. Thus Σ at fixed z^* and that at fixed ρ_{cg} have different temperature dependences. This is similar to what we know for the solvation in bulk liquids at fixed pressure and at fixed density: the solubility Σ of methane reaches a minimum at around 350 K under atmospheric pressure whereas Σ decreases monotonically at a fixed density of water. However, the conclusion one can derive from Fig. 3.5 is much robust. That is, the local solubility of nonpolar solutes in water or in simple fluids decreases with increasing T at *any* fixed density in the liquid-vapor interface, i.e., any density between the gas and liquid phases.

3.7 Summary

The main purpose of the present study is to understand the hydrophobic hydration of nonpolar solutes in the liquid-vapor interface of water in terms of the local solubility and its temperature dependence. We have calculated the local solubility $\Sigma(z)$, for a model aqueous solution of methane (methane/water) in the liquid-vapor equilibrium, from the MD simulation of pure water and the test-particle insertion method. For comparison we have also calculated $\Sigma(z)$ for a model krypton solution of methane (methane/krypton) and a model solution (hydrophobic LJ/LJ), both of which consist of an LJ solute and an LJ solvent but the latter LJ parameters are chosen such that the solvation is of hydrophobic character.

The local solubility profile $\Sigma(z)$ of methane through the water interface has a maximum on the vapor side of the equimolar surface and a minimum on the liquid side. The maximum is the surface adsorption of solutes and is commonly observed for aqueous and non-aqueous solutions. The minimum in $\Sigma(z)$ on the liquid side has been reported for various aqueous solutions [20, 23, 45]; no minimum is observed for the methane/krypton and hydrophobic LJ/LJ solutions. What we have found is that the minimum is more pronounced as temperature is decreased to a supercooled metastable state (Fig. 3.3). It was remarked that the growth of the minimum in $\Sigma(z)$ is correlated with the growth of layering structure in $\rho_B(z)$ of water on the liquid side of the interface. Since

we know the solubility of hydrophobic solutes in liquid water decreases with increasing the water density at fixed temperature, the minimum solubility in the interfacial region is caused by the layering structure right at the water interface. For all the systems the local solubility $\Sigma(z)$ at fixed z , smaller or larger than 1, decreases with increasing temperature except in the vapor region of the system. A difference between water and the LJ fluid is that the effect of temperature on Σ of methane in water is largest deep inside the liquid region while that of LJ solutes in LJ solvents is largest right at the interface where Σ is maximum (Fig. 3.3). A marked character of $\Sigma(z)$ for methane/water in comparison with that for hydrophobic LJ/LJ is that variation of $\Sigma(z)$ with z is much more rapid near the equimolar surface and Σ becomes smaller than 1 at less than a few angstroms to the liquid side.

We have examined the temperature dependence of Σ at fixed z and at fixed coarse-grained solvent density ρ_{cg} . There is a minimum of the local solubility as a function of T for methane/water and also for hydrophobic LJ/LJ at a fixed distance on the liquid side ($z^* = 4$). On the vapor side, Σ is nearly constant but slightly increases with T . On the other hand the local solubility at any given ρ_{cg} for all the systems decreases monotonically with increasing temperature. This is analogous to the relation between the temperature dependence of Σ of a hydrophobic solute in water at fixed pressure and that at fixed volume. What has been shown here is that the observation that the solubility decreases monotonically with temperature at fixed solvent density is true for *nonuniform* fluids where the density varies in space from the vapor to the liquid phase.

References

- [1] H. S. Frank and M. W. Evans. *J. Chem. Phys.*, **13**, 507 (1945).
- [2] G. Hummer, S. Garde, A. E. García, and L. R. Pratt. *Chem. Phys.*, **258**, 349 (2000).
- [3] N. Galamba. *J. Phys. Chem. B*, **117**(7), 2153–2159 (2013).
- [4] W. Blokzijl and m. B. F. N. Engberts. *Angew. Chem., Int. Ed.*, **32**, 1545 (1993).
- [5] P. Ball. *Chem. Rev.*, **108**, 74 (2008).
- [6] H. S. Ashbaugh and M. E. Paulaitis. *J. Am. Chem. Soc.*, **123**, 10721 (2001).
- [7] N. T. Southall, K. A. Dill, and A. D. J. Haymet. *J. Phys. Chem. B*, **106**, 521 (2002).

- [8] M. Lucas. *J. Phys. Chem.*, **80**, 359 (1976).
- [9] B. Lee. *Biopolymers*, **24**, 813 (1985).
- [10] B. Lee. *Biopolymers*, **31**, 993 (1991).
- [11] K. Koga. *Phys. Chem. Chem. Phys.*, **13**, 19749 (2011).
- [12] G. L. Richmond. *Chem. Rev.*, **102**, 2693 (2002).
- [13] K. Wolfrum, H. Graener, and A. Laubereau. *Chem. Phys. Lett.*, **213**, 41 (1993).
- [14] V. M. Kaganer, H. Möhwald, and P. Dutta. *Rev. Mod. Phys.*, **71**, 779 (1999).
- [15] G. Ma and H. C. Allen. *Langmuir*, **22**, 5341 (2006).
- [16] T. Rasing, Y. R. Shen, M. W. Kim, P. Valint, Jr., and J. Bock. *Phys. Rev. A*, **31**, 537 (1985).
- [17] E. Tyrode, C. M. Johnson, A. Kumpulainen, M. W. Rutland, and P. M. Claesson. *J. Am. Chem. Soc.*, **127**, 16848 (2005).
- [18] K. B. Eisenthal. *Chem. Rev.*, **96**, 1343 (1996).
- [19] Y. R. Shen. *Nature*, **337**, 519 (1989).
- [20] A. Pohorille and I. Benjamin. *J. Chem. Phys.*, **94**(8), 5599–5605 (1991).
- [21] P. Jedlovszky, I. Varga, and T. Gilányi. *J. Chem. Phys.*, **119**, 1731 (2003).
- [22] L. B. Pártay, P. Jedlovszky, P. N. M. Hoang, S. Picaud, and M. Mezei. *J. Phys. Chem. C*, **111**, 9407 (2007).
- [23] R. Vácha, P. Slavíček, M. Mucha, B. J. Finlayson-Pitts, and P. Jungwirth. *J. Phys. Chem. A*, **108**, 11573 (2004).
- [24] R. Vácha, P. Jungwirth, J. Chen, and K. Valsaraj. *Phys. Chem. Chem. Phys.*, **8**, 4461 (2006).
- [25] R. S. Taylor, D. Ray, and B. C. Garrett. *J. Phys. Chem. B*, **101**, 5473 (1997).

- [26] V. Venkateshwaran, S. Vembanur, and S. Garde. *Proc. Natl. Acad. Sci. U. S. A.*, **111**, 8729 (2014).
- [27] K. Abe and K. Koga. *J. Mol. Liq.*, **200**, 7 (2014).
- [28] B. Widom. *J. Stat. Phys.*, **19**, 563 (1978).
- [29] J. L. F. Abascal and C. Vega. *J. Chem. Phys.*, **123**, 234505 (2005).
- [30] J. O. Hirschfelder, C. F. Curtiss, and R. B. Bird. *Molecular theory of gases and liquids*. Wiley, New York (1954).
- [31] S. Nosé. *J. Chem. Phys.*, **81**, 511 (1984).
- [32] S. Nosé. *Mol. Phys.*, **52**, 255 (1984).
- [33] W. G. Hoover. *Phys. Rev. A*, **31**, 1695 (1985).
- [34] A. Trokhymchuk and J. Alejandre. *J. Chem. Phys.*, **111**, 8510 (1999).
- [35] M. Mecke, J. Winkelmann, and J. Fischer. *J. Chem. Phys.*, **107**, 9264 (1997).
- [36] L.-J. Chen. *J. Chem. Phys.*, **103**, 10214 (1995).
- [37] C. Ibergay, A. Ghoufi, F. Goujon, P. Ungerer, A. Boutin, B. Rousseau, and P. Malfreyt. *Phys. Rev. E*, **75**, 051602 (2007).
- [38] J. Wang, A. G. Kalinichev, and R. J. Kirkpatrick. *J. Phys. Chem. C*, **113**(25), 11077–11085 (2009).
- [39] L. X. Dang and T.-M. Chang. *J. Chem. Phys.*, **106**(19), 8149 (1997).
- [40] L. B. Pártay, G. Hantal, P. Jedlovsky, Á. Vincze, and G. Horvai. *J. Comput. Chem.*, **29**(6), 945–956 (2008).
- [41] A. P. Willard and D. Chandler. *J. Phys. Chem. B*, **114**(5), 1954–1958 (2010).
- [42] E. Chacón, M. Reinaldo-Falagán, E. Velasco, and P. Tarazona. *Phys. Rev. Lett.*, **87**, 166101 (2001).

- [43] E. Chacón and P. Tarazona. *Phys. Rev. Lett.*, **91**(16), 166103 (2003).
- [44] E. M. Fernández, E. Chacón, P. Tarazona, A. O. Parry, and C. Rascón. *Phys. Rev. Lett.*, **111**(9), 096104 (2013).
- [45] B. C. Garrett, G. K. Schenter, and A. Morita. *Chem. Rev.*, **106**, 1355 (2006).
- [46] R. Battino. Methane in water. In H. L. Clever and C. L. Young, editors, *IUPAC Solubility Data Series*, volume 27/28, pages 1–6. Pergamon, Oxford (1987).
- [47] R. F. Prini and R. Crovetto. *J. Phys. Chem. Ref. Data*, **18**, 1231 (1989).
- [48] B. Guillot and Y. Guissani. *J. Chem. Phys.*, **99**, 8075 (1993).
- [49] D. Paschek. *J. Chem. Phys.*, **120**, 6674 (2004).

Summary

In Chapter 1, freezing behavior in confined fluids is studied, specifically for a liquid monolayer adsorbed in a cylindrical pore. The main purpose is to examine the effect of pore diameter on the sharpness of continuous freezing. The monolayer is described by a nearest-neighbor lattice model which is a simpler version of Potts model and can be mapped to Ising model. The lattice geometry is a square net rolled on the surface of an infinitely long cylinder. The number m of lattice points in the rolling direction serves as a measure of the pore diameter. With decreasing temperature the model exhibits a phase change from orientation-disordered liquid state to orientation-ordered solid state (almost all molecules are in the state 1). The ratio ρ_1 of the average number of molecules in the state 1 to the total number of molecules is naturally chosen as an order parameter. The freezing behavior in the two-dimensional limit ($m \rightarrow \infty$) is either discontinuous or continuous freezing, depending on the model parameters, P and Q . The selected values, (1) $P = 2$, $Q = 2.2$ and (2) $P = 1$, $Q = 2.8$, correspond to discontinuous and continuous change in the two-dimensional limit, respectively. Using Monte Carlo simulation, the temperature dependence of ρ_1 for $m = 1, 2, \dots, 8$ is obtained. For case (1), continuous freezing is observed at $m = 1, 2, 4$. With increasing m , the sharpness of freezing increases so rapidly that a very sharp change indistinguishable from discontinuous change is observed at $m = 8$. Approaching discontinuous change by increasing m is not surprising but it is not trivial that the true discontinuous phase change, which is possible only at $m \rightarrow \infty$, is almost achieved at such a small value of m . For case (2), too, continuous freezing is observed and its sharpness increases with increasing m . Although the two-dimensional limit is now continuous change, the change in sharpness with m converges at $m \sim 8$. These results suggest that the pore diameter of several molecular diameters is sufficiently large for a liquid monolayer to exhibit as sharp freezing as its two-dimensional limit. This lattice model is further generalized by making the intermolecular interaction energy dependent on the direction of the pair (axial or rolling

direction). When the corresponding Ising model is ferromagnetic in the rolling direction ($P' > 0$) and antiferromagnetic in the axial direction ($P < 0$), a stable, intermediate state is found between the solid and liquid states. In the new phase, each set of m molecules in the rolling direction can be regarded as either liquid or solid state and the liquid-ring and solid-ring alternate along the axial direction.

In Chapters 2 and 3, solubility of small, spherical, and nonpolar molecules in the interfacial region between water and vapor phases is studied. The local quantity $\Sigma(z) = \exp(-\mu_{\text{ex}}(z)/kT)$ is adopted to evaluate the local solubility as a function of distance z from the interface. In both chapters, molecular dynamics simulation and test particle method are employed to calculate $\Sigma(z)$. Local solubility in the interface of simple liquids is also considered for comparison.

In Chapter 2, $\Sigma(z)$ at a fixed temperature near the triple point is obtained for various values of the ratio ε^* of the strength of Lennard-Jones (LJ) attraction between solute and solvent molecules to that between solvent molecules. For the LJ solvent, the form of $\Sigma(z)$ is sensitive to ε^* . For example, the maximum in $\Sigma(z)$, which is the manifestation of interface adsorption, is observed only when $\varepsilon^* < 1$. As ε^* increases, $\ln \Sigma(z)$ on the liquid-side ($z > 0$) changes its sign at $\varepsilon^* \sim 0.7$ from negative (low solubility) to positive (high solubility). For water, on the other hand, both interface adsorption and low solubility in liquid-side are observed for any $0.5 \leq \varepsilon^* \leq 1.5$. The rest of this chapter is devoted to answer the question whether the resulting lower solubility in water comes from the nature of interfacial structure of water. It is shown by test particle theory that the value of Σ is determined not only by the solvent structure, but also by the solvent density and ε/kT , the ratio of the solute-solvent attractive energy to the temperature. Based on this idea, a stepwise analysis is performed. In this analysis, the local solubility is compared at equal local solvent density ρ_{cg} , instead of equal z . First, the local solubilities Σ of LJ solute in the two solvents are compared with common ε^* at their triple point temperature. In this case, Σ for water is lower than that for the LJ solvent, at any fixed ρ_{cg} . Second, a higher value of ε^* is chosen for water so that ε/kT is common for the two solvents. This made the local solubility in water higher than in LJ solvent, at any fixed solvent densities. Therefore, it is concluded that when the solvent density and the effective solute-solvent attraction ε/kT is the same, the water structure has a higher ability of dissolving small, nonpolar molecules than the structure in simple liquids. Calculation of the probability of cavity formation revealed that this is partly because a sufficiently large spherical void for the solute to enter is found

more frequently in water than in simple liquids. The answer to the question above is that the lower solubility of nonpolar molecules in the interface of water is not due to the solvent structure of water. Water has, rather, an advantage with regard to the solvent structure, but this is overwhelmed by its disadvantage of having a higher value of the triple point temperature. A remarkable observation is that this is the case for any intermediate densities between those of homogeneous liquid and vapor phases. Finally, it is revealed that the probability of cavity formation is a universal function of a scaled solvent density for liquid-vapor interfaces of different fluids.

In Chapter 3, the effect of varying temperature on the local solubility is examined for realistic systems: methane in the liquid-vapor interface of water (methane/water) and methane in the interface of krypton (methane/krypton). In addition, one model system of an LJ particle in the interface of a LJ fluid (hydrophobic LJ/LJ) is considered. The solute-solvent LJ parameters of hydrophobic LJ/LJ are chosen from such parameter region that both the excess chemical potential of bulk LJ/LJ solution and its temperature derivative at fixed pressure are positive, which is characteristic of hydrophobic solvation in bulk water. The temperature ranges examined are $243 \text{ K} \leq T \leq 373 \text{ K}$ for methane/water, $0.6 \leq T^* \leq 1.0$ for methane/krypton, and $0.5 \leq T^* \leq 1.0$ for hydrophobic LJ/LJ, all of which include supercooled states. First, the temperature effect on the shape of $\Sigma(z)$ is examined. For all the systems, the maximum in $\Sigma(z)$ (i.e. interface adsorption) is observed near the triple point temperature and the maximum value decreases with increasing temperature. Several features of local solubility $\Sigma(z)$ is correlated with the density profile of the solvent, $\rho_B(z)$. As temperature increases, both $\Sigma(z)$ and $\rho_B(z)$ vary more slowly with z . Also, only methane/water exhibits a minimum in $\Sigma(z)$, the position of which is close to that of the first maximum of the oscillation found in $\rho_B(z)$ of water. The difference between Σ at the minimum and at deeply inside the liquid phase increases with decreasing temperature, while the maximum in $\rho_B(z)$ is more pronounced as temperature decreases. These two observations suggest that the minimum in $\Sigma(z)$ is mainly caused by the layering structure of the interfacial water. The effect of temperature is largest in deeply inside the liquid phase for methane/water, while it is largest around the maximum of $\Sigma(z)$ ($z \simeq 0$) for the other two systems. Second, the temperature dependence of Σ is examined at two different conditions: fixed z and fixed solvent density ρ_{cg} . For fixed z condition, the temperature dependence of Σ on the vapor-side ($z < 0$) is similar for all systems, while only methane/water and hydrophobic LJ/LJ exhibit a minimum for z on the liquid-side ($z > 0$). The latter indicates that the minimum of

solubility with respect to temperature, which is often considered as a characteristic feature of aqueous solutions of hydrophobic molecules, is not a specific feature of water but also is shared with simple liquids. For fixed-density condition, Σ decreases monotonically with temperature for all the systems and for any value of ρ_{cg} between the vapor and liquid densities of the solvent. Monotonic decrease of solubility with increasing temperature at fixed solvent density is already confirmed for homogeneous solutions. The present study showed that this is also true for the solvation in the inhomogeneous region between the vapor and liquid phases.

List of Publications

Kiharu Abe and Kenichiro Koga,

“Model of Freezing Behavior of Liquid Monolayers Adsorbed in Cylindrical Pores”

The Journal of Physical Society of Japan, **81**, SA021 (2012).

Kiharu Abe and Kenichiro Koga,

“Local solubility of nonpolar molecules in the liquid-vapor interfaces of water and simple liquids”

Journal of Molecular Liquids, **200**, 7 (2014).

Kiharu Abe, Tomonari Sumi, and Kenichiro Koga,

“Temperature dependence of local solubility of hydrophobic molecules in the liquid-vapor interface of water”

The Journal of Chemical Physics, **141**, 18C516 (2014).

Acknowledgments

I would like to express my sincere appreciation to my supervisor Prof. Kenichiro Koga. I express a great respect to him and owe him a debt of gratitude, since I could learn the philosophy of theoretical approach and essential attitude as a scientific researcher. I wish to express my deep gratitude to Prof. Tomonari Sumi for helping me with valuable discussions.

I am deeply grateful to Prof. Ryo Akiyama for making considerable efforts for organizing the publication of the proceedings of the Mini-Symposium on Liquids, which gave me my first opportunity to write a paper during the master course.

I am indebted to all of my colleagues in the theoretical physical chemistry group and the laboratory of theoretical chemistry for stimulating and helpful discussions.

I wish to conclude with my most heartfelt gratitude to my parents Junko Abe and Norihide Abe for their continuing supports and deep understanding.

Okayama

January 2015

Kiharu Abe